Three-Dimensional Modeling of Quasi-Homologous Solar Jets

E. Pariat

LESIA, Observatoire de Paris, CNRS, UPMC, Université Paris Diderot, 92190 Meudon, France

`etienne.pariat@obspm.fr`

and

S. K. Antiochos

Space Weather Laboratory, NASA Goddard Space Flight Center, Greenbelt, MD 20771, USA

and

C. R. DeVore

Laboratory for Computational Physics and Fluid Dynamics, Naval Research Laboratory, Washington, DC 20375, USA

ABSTRACT

Recent solar observations (e.g., obtained with *Hinode* and *STEREO*) have revealed that coronal jets are a more frequent phenomenon than previously believed. This higher frequency results, in part, from the fact that jets exhibit a homologous behavior: successive jets recur at the same location with similar morphological features. We present the results of three-dimensional (3D) numerical simulations of our model for coronal jets. This study demonstrates the ability of the model to generate recurrent 3D untwisting quasi-homologous jets when a stress is constantly applied at the photospheric boundary. The homology results from the property of the 3D null-point system to relax to a state topologically similar to its initial configuration. In addition, we find two distinct regimes of reconnection in the simulations: an impulsive 3D mode involving a helical rotating current sheet that generates the jet, and a quasi-steady mode that occurs in a 2D-like current sheet located along the fan between the sheared spines. We argue that these different regimes can explain the observed link between jets and plumes.

Subject headings: Sun: corona—Sun: magnetic fields

1. INTRODUCTION

Jets are a very common active phenomenon of the solar atmosphere usually defined as a collimated and mainly radially extended source emitting at a given wavelength (although some jets are seen in absorption; e.g., Hα surges). The Sun exhibits jet-like events on a vast range of scales: photospheric spicules (e.g. Tziotziou et al. 2003; Pontieu et al. 2007); chromospheric Hα surges (e.g. Schmahl 1981; Schmieder et al. 1995; Canfield et al. 1996; Chen et al. 2008); chromospheric Ca II H jets (e.g. Nishizuka et al. 2008); coronal EUV microjets (Gurman et al. 1998); coronal X-ray jets (e.g. Shibata et al. 1992; Savcheva et al. 2007; Kamio et al. 2007); macrospicules (Yamauchi et al. 2004); and white-light polar jets (Wang et al. 1998; Wang & Sheeley 2002). A particular jet event sometimes is observed in different wavelengths (Schmieder et al. 1995; Canfield et al. 1996; Alexander & Fletcher 1999; Chifor et al. 2008a; Chen et al. 2008), although its various manifestations may not be completely co-temporal and/or co-spatial (Chae et al. 1999; Liu & Kurokawa 2004; Jiang et al. 2007). Such observations may give insight into different features of the jet phenomenon. All of these structures, despite their different sizes, present common characteristics suggesting that a common mechanism is responsible for the ubiquitous jet-like events: magnetic reconnection (Shibata et al. 2007).

Several lines of argument suggest an important role for reconnection. The largest events, the X-ray jets, are usually associated with micro-flares and X-ray bright-point brightenings (Shibata et al. 1992, 1994; Shimojo et al. 1996; Shimojo & Shibata 2000), which are widely believed to be due to magnetic reconnection. The energy and temperature of the jet are strongly correlated with the corresponding quantities in the microflare, indicating a common mechanism for both phenomena. The energy of the X-ray jets is estimated to be of the order of 10^{20}–10^{22} J (Shimojo & Shibata 2000); thus, the source of the energy is likely to be magnetic. This energy has to be released on a relatively short time scale, of the order of several minutes, much smaller than that for energy injection in the corona. Shimojo & Shibata (2000) showed that the thermal energy emitted by the jet is related to the magnetic flux at its chromospheric footpoint. In addition, the distribution of the magnetic field is usually multipolar (Shimojo et al. 1998), which is consistent with the magnetic reconnection model. Magnetic extrapolation of the sources of a UV jet (Fletcher et al. 2001) and more recently of an X-ray jet (Moreno-Insertis et al. 2008) have associated the classical anemone structure of the jets (Shibata et al. 1992; Shimojo et al. 1996) with an underlying 3D magnetic null-point topology, a strongly preferred site for reconnection to occur (Pontin et al. 2004; Pontin & Galsgaard 2007; Priest & Pontin 2009).

Magnetohydrodynamic (MHD) numerical simulations have confirmed that magnetic reconnection at a null point can explain numerous observable properties of jets (Yokoyama

& Shibata 1995, 1996; Miyagoshi & Yokoyama 2004; Archontis et al. 2004, 2005, 2007; Moreno-Insertis et al. 2008; Gontikakis et al. 2009). These simulations have shown that the plasma acceleration due to slingshot relaxation of the reconnected field lines is not directly responsible for the thermodynamic and kinematic properties of the X-ray jets. Rather, the jet emission is due to the evaporative flow of plasma heated by the reconnection process. However, this process cannot account for the very high velocities (of the order of the Alfvén speed) and the wave-like behavior observed in some jets (Kim et al. 2001; Cirtain et al. 2007; Nishizuka et al. 2008).

Recently, we (Pariat et al. 2009, hereafter PAD09) reported 3D numerical simulations demonstrating that impulsive 3D reconnection at a null point can generate a nonlinear Alfvénic wave, which transfers away the stored magnetic energy and helicity along reconnected field lines. This jet mechanism elaborates the "magnetic twist jet" (Shibata et al. 1997) based on the early simulations of Shibata & Uchida (1985, 1986), although the term "untwisting jet" would be more appropriate. Török et al. (2009) simulated an emerging twisted flux tube interacting with the large scale coronal field, which generated a similar untwisting nonlinear wave by null-point reconnection and induced the subsequent formation of the classical anemone/null-point topology.

Our model (PAD09) also readily explains the helical structure regularly observed in surges and jets, in particular the largest events (Shibata et al. 1992; Gu et al. 1994; Canfield et al. 1996; Alexander & Fletcher 1999; Harrison et al. 2001; Kim et al. 2001; Jibben & Canfield 2004; Jiang et al. 2007). Jibben & Canfield (2004) noted that the sign of the source helicity agreed with the sense of rotation of most of the 47 surges they studied. Recently, the groundbreaking stereoscopic capabilities of the *STEREO* mission (Kaiser et al. 2008) enabled direct insights into the helical structure of jets. The PAD09 model succeeded in reproducing the 3D helical structure of a particular event observed in the UV (Patsourakos et al. 2008). A broader study of the 3D geometrical properties of coronal jets revealed that, with the present spatial resolution of *STEREO*, about 40% of the jets exhibit clear helical structure (Nistico et al. 2009). This ratio is much higher than the 14% found from lower-resolution observations obtained with the *Hinode* XRT instrument (Savcheva et al. 2009).

Perhaps the most persuasive argument for the importance of reconnection in jets results from the simulations of Rachmeler et al. (2010) using the purely ideal magnetohydrostatic solver FLUX (Deforest & Kankelborg 2007). Starting with the same initial configuration as PAD09, Rachmeler et al. (2010) showed that jets were not generated when reconnection was forbidden, although the initial evolution was similar to PAD09. Comparison of the two calculations demonstrates convincingly that magnetic reconnection is indeed the essential mechanism for jet generation. Once reconnection occurs, magnetic field-line slingshot,

evaporative flow, and untwisting act simultaneously. These processes compete and lead to complementary observational properties of the jets. Each process may be more or less important depending upon the magnetic geometry of the source: size, flux distribution, location of the null, and any symmetry properties.

One property of jets that has not been addressed previously by numerical simulation is their tendency to recur at a single location. The fact that X-ray jets occur much more frequently than previously believed (Cirtain et al. 2007; Savcheva et al. 2007) is partly due to this property. Recurring jets have been noted in numerous studies of surges (e.g. Asai et al. 2001; Chen et al. 2008), EUV jets (Chae et al. 1999; Wang et al. 2006; Jiang et al. 2007; Gontikakis et al. 2009), and X-ray jets (Kim et al. 2001; Chifor et al. 2008a,b). Wang et al. (2006) reported EUV jets recurring over a duration of a day or more. Jiang et al. (2007) found an average time of 70 min between recurring EUV jets having a length of 50 Mm while Kim et al. (2001) noted a 3-4 hr delay between X-ray jets having a size of 70 Mm. Asai et al. (2001) reported eight successive, relatively uniform surges of length 17 Mm and mean recurrence period of 42 min. One particular magnetic structure (Chen et al. 2008) generated seven surges whose lengths ranged from 38 Mm to 214 Mm and time delays varied from 11 min to 74 min. It is worth noting from their data that the projected length of a jet seems to be related to the time delay following the previous surge.

A recent detailed study of a recurring coronal jet using the instruments on-board *Hinode* Chifor et al. (2008a) showed that at least four successive jets were triggered and exhibited similar structure. Indeed, recurring jet-like events tend to be homologous, i.e., the successive jets assume the same characteristic geometry as the first (Jiang et al. 2007; Chifor et al. 2008a; Chen et al. 2008). Recurrent jets are always elongated and collimated in the same direction, and the structure at their footpoints is usually similar. Although the intensity and spatial extent of the emission can vary (Chen et al. 2008; Chifor et al. 2008a), the overall morphology is preserved.

A robust model of jets must be able to account for this homologous property, which seems to be ubiquitous, i.e., independent of the scale of the jet and its associated magnetic structure. The aim of the present paper is to demonstrate that our model (PAD09) can produce recurrent jets and to determine the underlying cause of this behavior. DeVore & Antiochos (2008) found a similar homologous property in their simulations of successive confined filament eruptions via 3D magnetic breakout. They demonstrated that continual stressing at the base of a quadrupolar structure with a null point periodically disrupts and then reforms the magnetic geometry, thus self-consistently generating the homologous sequence. Also, during the preparation of this paper, we learned that Archontis et al. (2010) have developed an oscillatory-reconnection model that attempts to explain the active-region

recurrent jets observed by Gontikakis et al. (2009).

Our paper is organized as follows. In § 2, we summarize the physical and numerical approximations behind the simulations. The evolution of the energies, connectivity, and other properties of four quasi-homologous recurrent jets generated by our model are presented in § 3. We then discuss the origin of the homologous property (§ 4.1), the existence of two distinct regimes of reconnection (§ 4.2), and the implications of our results for the relation between jets and plumes (§ 4.3).

2. NUMERICAL MODEL

The simulations presented in this paper extend our previous work in PAD09, where the model is described more comprehensively. In brief, the calculations have been performed with the *Adaptively Refined Magnetohydrodynamic Solver* (*ARMS*), whose flux-corrected transport algorithms are based on those presented in DeVore (1991). A Cartesian domain, with x and y the horizontal axes and z the vertical axis, is assumed. The time-dependent equations of ideal MHD, with the magnetic forces expressed in the Lorentz form, are solved on a dynamically solution-adaptive grid managed by the toolkit *PARAMESH* (MacNeice et al. 2000). Our nonuniform initial grid is identical to that presented in Figure 1 of PAD09.

This grid refines and derefines adaptively during the simulation, governed by the ratio of the electric current density to the magnetic field relative to the local grid spacing. The adaptive meshing adjusts the grid to resolve as finely as possible the thin current layers that drive and control the reconnection process. No explicit resistive MHD terms are included in the model. Numerical diffusion provides an effective resistivity, in particular where the gradients of the magnetic field are strong, i.e., at the current sheets where the grid is most highly refined.

The domain is filled with a highly conducting, low-pressure coronal plasma. For maximum generality, we use non-dimensional units; however, a comparison with actual coronal scales can be found in § 5.2 of PAD09. Our initial thermal pressure is uniform ($P = 1 \times 10^{-2}$), as is the initial mass density ($\rho = 1$). We assume an ideal plasma equation of state. The temperature is initially uniform, $T = P/(\rho R) = 1$, where $R = 1 \times 10^{-2}$ is the gas constant.

The initial magnetic configuration is composed of two flux systems. First, a region of closed, concentrated field is created by an embedded dipole of strength m_0 ($\mu_0 m_0/4\pi = 25$), oriented vertically and positioned below the bottom coronal boundary at $(0, 0, z_0 = -1.5)$. The surrounding open magnetic field is uniform, $\mathbf{B}_v = -B_v \cos\theta\, \mathbf{e}_z + B_v \sin\theta\, \mathbf{e}_y$ with $B_v = 1$. The resultant peak Alfvén speed is $c_A = 0.28$, while the minimum plasma beta – ratio of

thermal to magnetic pressure – is $\beta = 0.25$. (We note that a rerun of the PAD09 simulations using $\beta = 0.06$ resulted in no significant differences with our previously reported results). An important change from the simulations of PAD09 is that the open field here is inclined relative to the vertical $\mathbf{e}_z$ by the angle θ. As in the single-jet simulations in Patsourakos et al. (2008), we set $\theta = 10°$. The total vertical magnetic field at the photospheric level therefore is

$$B_z(x, y, 0) = \frac{\mu_0 m_0}{4\pi} \frac{2z_0^2 - (x^2 + y^2)}{(x^2 + y^2 + z_0^2)^{5/2}} - B_v \cos\theta. \tag{1}$$

The resulting topological structure is presented in Figure 1. Since $\mu_0 m_0 / 2\pi |z_0|^3 >> B_v$, the flux distribution in the embedded dipole at the photospheric level is only very slightly changed relative to PAD09. However, the overall magnetic structure is no longer axisymmetric. The 3D null point with its associated fan surface and two spine lines is preserved, but the outer spine follows the general direction of the open field and so is inclined by $10°$. The 3D null point is displaced slightly along $-\mathbf{e}_y$ relative to the symmetry axis of the fan surface, positioned now at $(0, -0.42, 2.15)$. Although small, this displacement implies that magnetic reconnection is not inhibited by the initial axisymmetry that prevailed in PAD09. As we will see in § 3.1, however, the symmetry-breaking is only mildly consequential: although a current sheet forms quickly after the boundary driving starts, as in PAD09, the reconnection rate nevertheless remains quite small over an extended time, and the overall evolution is very similar to that in PAD09.

We assume the same boundary conditions as PAD09, i.e., closed on the four sides and open at the top. At the bottom boundary, line-tied conditions are used to emulate the lower layers of the solar atmosphere and forcing motions are imposed to drive the magnetic evolution. The vertical field is driven by imposed slow twisting motions restricted to the positive polarity, as in PAD09. This applied flow follows the contours of B_z, so as to leave its surface distribution unchanged in time. As was true in DeVore & Antiochos (2008), therefore, at all times during the simulation the minimum magnetic energy is fixed and equal to that of the initial potential field. This allows us to study directly the accumulated free magnetic energy E_f, $E_f(t) = E_m(t) - E_m(t = 0)$, in place of the total magnetic energy E_m.

The imposed tangential velocity $\mathbf{v}_\perp(x, y, z = 0)$ is given by Equation (7) of PAD09. However, unlike in PAD09, after the boundary flows are accelerated smoothly from rest, they are maintained continuously at maximum speed. The multiplicative temporal factor thus takes the form

$$f(t) = \begin{cases} 0 & \text{for} \quad t \leq t_l \\ \frac{1}{2}\left(1 - \cos\left(\pi \frac{t - t_l}{t_r - t_l}\right)\right) & \text{for} \quad t \in [t_l, t_r] \\ 1 & \text{for} \quad t \geq t_r \end{cases} \tag{2}$$

Note that $\mathbf{v}_\perp$ vanishes at all other surface locations. This prescribed velocity field imparts a clockwise rotation (seen from above) to the positive central polarity, therefore injecting positive helicity into the closed-field region and forming a clockwise whorl.

We performed two runs. The first, which will be thoroughly described in § 3, has an applied driving amplitude $v_0 = 1 \times 10^{-5}$ and time constants $t_l = 100$ and $t_r = 400$. In the second, we set $t_l = 100$, $t_r = 700$, and $v_0 = 2 \times 10^{-5}$. The eventual constant-speed driving thus is twice as fast in the second simulation relative to the first, so hereafter we will refer to them as the "fast" and "slow" runs, respectively. The change in $t_r - t_l$ keeps the peak acceleration the same in the two simulations. The rotation rates Ω at radius $r = 1$ from the flow center are presented in Figure 2. Note that even for the "fast" simulation, the prescribed velocity is about half what we used in PAD09, corresponding to less than 5% of the Alfvén speed. The corresponding theoretical numbers of turns given to field lines anchored at $r = 1$ also are plotted in Figure 2.

3. RECURRING JETS

After the initial ramping-up phase, the magnetic configuration is forced continuously at its bottom boundary. The reaction of the system to this constant driving is highly nonlinear, however, and exhibits a quasi-periodic pattern. Over the course of the simulation, four quasi-homologous jets are generated successively through a process very similar to that described in PAD09. Impulsive 3D null-point reconnection triggers a rapid untwisting of previously closed helical field lines as they reconnect with open flux.

3.1. Energy Evolution

The evolution of the free magnetic energy E_f and kinetic energy E_{kin} in the system throughout its evolution are presented in Figure 3. This figure, in essence, exhibits the same properties as that of the energy of the breakout filament eruptions simulated by DeVore & Antiochos (2008, see Figure 4 therein). The quasi-periodic variations are one important indicator of the homologous behavior of the magnetic configuration simulated here. In contrast to DeVore & Antiochos (2008), our free energy E_f does not accumulate secularly, because the magnetic and kinetic energies are free to escape through the top boundary of our open domain. Note, however, that this result requires that the reconnection be very efficient at releasing all the energy injected by the photospheric motions. The free energy (*dashed line*) initially increases approximately linearly, at a dimensionless rate of 3.4×10^{-2}.

Four quasi-periodic variations are then observed between $t_r = 700$ and $t_e = 5430$, due to the triggering of the four recurrent jets. The simulation was halted arbitrarily at time t_e. We emphasize that no incipient instability was observed at this time and the system remained well behaved, and we believe that the quasi-periodic evolution displayed thus far would continue if the simulation were resumed.

The kinetic energy in Figure 3 (*solid line*) presents four peaks, each of them resulting from a burst of accelerated plasma as an untwisting jet is generated. The evolution of the system can be decomposed into a succession of jet cycles. Defining a cycle as the interval between two consecutive local minima[1] of the free magnetic energy, $(t_{\mathrm{Ef,min}}, E_{\mathrm{f,min}})$, four complete cycles can be observed during the simulation. Each cycle can be decomposed further into two phases: the first, called the energy-storage phase hereafter, is characterized by an increase in E_{f}; and the second, the energy-release phase, by a decrease in E_{f}. The changeover between these two phases therefore occurs at the times $t_{\mathrm{Ef,max}}$ of local maxima $E_{\mathrm{f,max}}$ in the magnetic energy. The different values obtained for the different jets are presented in Table 1, along with the period Δt_{max} (resp. Δt_{min}) between two consecutive maxima (resp. minima); the amplitude ΔE_{kin} of the kinetic-energy variation; the decrease (release) of energy $\Delta_R E_{\mathrm{f}} = E_{\mathrm{f,min}}$ - $E_{\mathrm{f,max}}$ between a free-energy minimum and the preceding maximum; and the increase (storage) of energy $\Delta_S E_{\mathrm{f}} = E_{\mathrm{f,max}}$ - $E_{\mathrm{f,min}}$ between an energy maximum and the previous minimum.

Initially, the evolution of the energies is similar to that found in PAD09. The imposed footpoint motions are slow, so that the kinetic energy remains very small even as the free magnetic energy begins to accumulate (cf. Figure 3) and the twisting induces an accelerating expansion of the closed magnetic flux. In contrast to our earlier work, however, the kinetic energy enters a phase of rather rapid increase between times $t \approx 1000$ and $t_{\mathrm{Ef,max,1}} = 1440$, at the onset of the first jet (cf. Fig. 5 of PAD09). As we will see below in § 4.2, this reflects acceleration of plasma by magnetic reconnection across the thin current sheet that develops between twisted closed flux and untwisted open flux at the fan separatrix. In PAD09, this reconnection was inhibited by the axisymmetry of the configuration. Even here, however, the reconnection rate remains small, little flux reconnects, and a relatively small amount of magnetic energy is transformed into kinetic energy until the impulsive jet occurs.

The principal fluctuations of E_{kin} are directly related to the variations of E_{f}: the four bursts in E_{kin} occur simultaneously with the four fast decreases in E_{f}. As shown in Figure

---

[1]Given this definition the first cycle appears a bit peculiar because of the initial energization. An alternative definition would be to define a cycle between two consecutive maxima. However, in that case only three full cycles would have been observed. The first definition emphasizes the jet as the central feature of a cycle.

4, after $t \approx 500$, the E_{kin} presents the same variation as does the negative time derivative of the free magnetic energy, $-dE_{\mathrm{f}}/dt$. This correlation illustrates that E_{kin} results from the transformation of the stored free energy E_{f}. The correspondence is particularly good during the energy-release phase, just after the triggering of each jet at time $t_{\mathrm{Ef,max}}$. The burst of kinetic energy is due directly to the reconfiguration of the magnetic field by reconnection, which generates the quasi-homologous untwisting jets (cf. § 3.3). Because the top boundary is open, a large portion of the magnetic energy carried by the jet is subsequently ejected out of the domain, enhancing the decrease in E_{f}. An associated decrease in E_{kin} is observed, also, due to both the ejection of the jet out of the domain and the slowing of the reconnection process at the current sheet.

At some time $t_{\mathrm{Ef,min}}$, a new cycle starts as injection of free energy due to the imposed boundary motions becomes the dominant process and E_{f} resumes its upward trend. The time derivative of the magnetic energy gradually ascends to its previous maximum value of 3.4×10^{-2} driven by the boundary motions. Meanwhile, the field geometry relaxes to its initial topological configuration in response to quasi-steady reconnections across the current sheet at the fan separatrix (cf. § 3.3). As the sheet dissipates, reconnection diminishes and the kinetic energy E_{kin} continues to decrease. Simultaneously, the injection of twist into the closed field continuously augments the free magnetic energy E_{f}. The system eventually reaches the critical stage at which a new untwisting jet is generated.

3.2. Cycle Characteristics

While our recurrent jets present strong quantitative similarities, their characteristics vary slightly from one cycle to the next (cf. Table 1). The very small number of recurrent jets obtained in the simulation do not admit of a meaningful statistical analysis, but a few conclusions can be drawn nonetheless. The first important result is that the jets occur for a stored free magnetic energy ranging from just 24 to 31 units; in the axisymmetric case in PAD09, the jet was triggered only at the much higher threshold energy of 51 units. Evidently, the free energy required for jet onset is substantially reduced when the symmetry is broken from the beginning, rather than having to be broken via an ideal kink mode as in PAD09 (cf. Rachmeler et al. 2010). We find that the free energy $\Delta_S E_{\mathrm{f}}$ accumulated between an energy minimum and the succeeding maximum vary significantly from cycle to cycle. This suggests that there may be no single, unique energy threshold for triggering our jets. However, $\Delta_S E_{\mathrm{f}}$ gives only partial information about the actual energy stored since the imposed motions continuously inject free energy even as each jet is released. Whereas in PAD09 83% of the free magnetic energy eventually was released, the ratio $\Delta_S E_{\mathrm{f}}/E_{\mathrm{f}}$ averages

47% for our four recurrent jets. The relatively fast, ongoing energy injection does not allow the system to relax fully to a new equilibrium state (cf. § 4.1). When the minimum energy $E_{\mathrm{f,min}}$ is reached, significant magnetic energy and helicity already have been injected into the still-relaxing closed-flux domain (cf. § 3.3).

By computing the Poynting flux through the bottom boundary, we determined the accumulated energy injected at the time of onset of each jet, obtaining [35, 64, 95, 128] respectively at the four times $t_{\mathrm{Ef,max}}$. The energy injected prior to initiation of the first jet slightly exceeds the free energy $E_{\mathrm{f,max,1}} = 32$ actually present in the system at that time (cf. Table 1). The difference reflects the free energy dissipated at the current sheet that forms before jet onset (cf. § 4.2). The running differences of the injected energies provide an estimate of the free energy available to power each jet. Even these values are only approximate, since some energy is injected directly onto field lines that temporarily open during the untwisting jets, and energy also is lost due to dissipation at the current sheet. Thus, an upper bound for the energy available to power each jet is [35, 29, 31, 33]. These values are relatively uniform, and thus do not preclude the existence of a fixed threshold for energy and helicity needed to trigger the jets.

Similarly, by computing the helicity flux at the bottom boundary (cf. PAD09) using the G_θ method (defined in Pariat et al. 2005), we have determined upper bounds for the magnetic helicity injected and available within the closed flux for each jet: [826, 656, 725, 778]. Dividing these values by the square of the magnetic flux in the closed polarity, $\Phi = 30$, gives estimates of the average number of turns on those field lines at jet onset. We obtained 0.85 ± 0.1 turns around the central spine, considerably smaller than the 1.3 turns found in PAD09.

This result is to be expected given the difference in the physical configuration between the two cases. As described in PAD09, the axial symmetry forbids any reconnection; hence, the system had to accumulate enough free energy so as to induce an ideal kink mode enabling fast 3D reconnection (Rachmeler et al. 2010). In the present case the system is 3D at the outset, so a current sheet forms at the deformed null and reconnection begins early in the evolution. This reconnection, however, is too slow to prevent the accumulation of free energy, as is evident from Figure 3. The key point, however, is that the system now has access to resistive instabilities, in particular the resistive kink, so that instability can set in at a lower free energy threshold. Of course, the instability is less explosive than in the axisymmetric case of PAD09; nevertheless, sufficient energy is released on a time scale short enough to account for observed coronal jets. We conclude that the geometry of the source structure, as determined by the inclination of the open field, plays a key role in the trigger mechanism. Preliminary simulations suggest that so long as the open field remains roughly vertical ($\theta \leq 30°$), however, the qualitative behavior of the untwisting jet itself remains

similar to that described in this paper.

Other features of the data in Table 1 include a secular decrease in the energy maximum $E_{f,max}$ prior to each jet; an oscillation in the energy minimum $E_{f,min}$ following each jet; and gradual increases in the period of the jet cycle as indicated by Δt_{max} and Δt_{min}. All of these changes plausibly reflect an ongoing evolution toward asymptotic periodic behavior of the system, as the memory of the initial conditions and the influence of other transients erode over time. Alternatively, there may be chaotic aspects to the dynamics of this highly nonlinear system that preclude its convergence to a perfectly homologous state. Determining which of these alternatives is correct would require running our system for many eruptions, which is unjustified given that homologous jets are observed to undergo only a few eruptions.

3.3. Evolution of the Connectivity

As the energy evolution suggests, the different jets present strong morphological similarities that confirm their homologous character. As observed in the confined eruptions of DeVore & Antiochos (2008), the quasi-homology of the jets is apparent through the evolution of the magnetic field-line connectivity presented in Figures 5, 6, and 7. These figures illustrate the topological structure of the jets at different times: each row corresponds to a single jet while each column corresponds to a particular stage of the jet generation. In every panel, the field lines are plotted from the same footpoints, located along the y axis at the bottom boundary within the negative polarity, which remain fixed in time since no boundary motions are applied there. Those field lines drawn in white initially belong to the open domain, while those drawn in red initially belong to the closed domain. Also shown are black isocontours of the 2D distribution of the electric currents, in the yz plane at $x = 0$, which indicate the location of the intense current sheets. Before detailing the evolution of the connectivity, we note that the graphic outputs of the simulations were obtained at a cadence ($\Delta t = 50$) which is sometimes longer than the evolutionary time scale of the simulation. Thus, at each stage in the cycle, although the times have been selected to represent best the homologous character of the jets, some minor differences in connectivity can be observed between the different panels because of the discrete subsampling interval used.

These figures show that at the equivalent stage of each jet cycle, the connectivity follows the same pattern for each jet, revealing the quasi-homologous property. Although no features are completely conserved between the jets, it is particularly notable that the third jet is more or less mirror-symmetric relative to the others. The first, second and fourth jets present identical topological evolution, but the third jet is significantly different. One interpretation is that some time is required to establish an approximately periodic behavior beginning

from the initial potential magnetic field. The system may not have had time to relax fully following the first jet in the sequence, and a nearly periodic behavior is established only at the time of energy maximum preceding the onset of the second jet (Fig. 5, second row, right column). Thereafter, a cyclical evolution of the field topology might lead to alternating left/right mirror-symmetric jets, and a jet 5 in the continued sequence could exhibit the same (mirror) symmetry as jet 3. Many jet cycles would need to be generated to test this hypothesis thoroughly. In any case, it is clear that the general configuration of the field at the onset of the jet has a dominant influence on its symmetry.

The left panel of Figure 5 displays the connectivity at times $t = 1250, 2250, 3350,$ and 4200, respectively, for the four successive jets during the approach to energy maximum. In the right panel, the connectivity is shown when the system just reaches the local maximum energy $E_{f,max}$. Significant reconnection occurs between those two times, as can be seen by the large number of field lines whose connectivity changes. As stated earlier, the jet initiation begins at the later time. Indeed, in a perfectly homologous system $t_{Ef,max}$ corresponds to the time at which the energy injected at the footpoints since the previous jet matches the energy to be released in the following jet. Visual examination of the intervening graphical datasets shows that a large fraction of the closed flux opens up by times $t = 1300, 2300, 3400,$ and 4250, respectively, prior to onset of the four jets. The configurations plotted in the left column of Figure 5 correspond to the pre-jet stage, at which time a substantial amount of twist has been injected into the closed field but the jet has not yet been triggered.

We note that at time $t = 2250$, prior to the second jet (1st column, 2nd row), several red field lines (initially closed) remain open. This is the principal evidence that the system was far from being relaxed completely following the first jet. Subsequently, a configuration is reached prior to each jet in which all red field lines are closed (1st column, 3rd and 4th rows). We observe for every jet that some white field lines, which originally belonged to the open domain, are now closed. This indicates that prior to jet onset, some reconnection occurs. Those reconfigured white field lines reconnected with closed field lines whose footpoints are located out of the yz plane, along the x axis (not represented in Fig. 5). This emphasizes the fundamentally 3D nature of the process. At this stage of the jet evolution, the reconnection rate remains relatively low and only a small amount of flux has reconnected, leading to a small enhancement of the kinetic energy (see § 3.1).

These early reconnections occur even for the first jet in the sequence; this is an important contrast with the PAD09 simulations. They are associated with the thin current sheet that develops on the left side of the closed-flux region at time $t = 1250$. The appearance of this current sheet, located near the null point and extending mainly in the $-y$ direction, further confirms that the axisymmetric configuration adopted in PAD09 efficiently inhibits

the development of current sheets. Quasi-steady reconnection at such current sheets in asymmetric configurations may be able to explain the plumes that sometimes develop prior to jets (cf. § 4.2).

At times $t_{\mathrm{Ef,max}}$ (right column of Fig. 5) the topological patterns displayed by jets 1, 2, and 4 are very similar. For these jets, white field lines on the left side $(-y)$ are now closed while red field lines on the right side $(+y)$ are now open. Some of the red field lines on the left side $(-y)$ also are open, but thread around the periphery of the closed-flux region to join with the open field on the right side of the outer spine. These field lines appear highly twisted at their lower ends and untwisted at their upper ends. The stage is set for a torsional wave to redistribute the twist from the bottom to the top of the domain, thereby generating the jet. Topologically, jet 3 is simply a left/right mirror image of its proceeding and following jets 2 and 4.

Each developing jet source contains an intense current sheet located at the separatrix between the open and closed fields. In Figure 5, only a section through the yz plane is plotted and so two thin current sheets seem to be present. However, these segments in fact are part of a single 3D current sheet that spirals down in a counterclockwise sense from the spine line at the top along the fan to the bottom surface (see § 4.2). The currents are particularly intense in the region where the rotation angle between the open and closed fields is the highest, as expected by Ampère's law.

On the right side of the closed system (in jets 1, 2, and 4; left side in jet 3), the field lines are almost horizontal along the fan. This is due to the helical shape of the closed field lines, which present a strong inclination relative to the open field lines that are mostly vertical. Note also that the (red) open field lines that have reconnected did not do so in the yz plane where they resided initially. The reconnection is inherently fully 3D, involving field lines distributed all along the fan surface. For example, the red field lines that are now open have reconnected with field lines located in the $+x$ domain (the near half-space relative to the viewer in Fig. 5) for jets 1, 2, and 4.

Figure 6 displays the topological structure during the generation and ejection of the untwisting jet. The four panels in the left column correspond respectively to times $t = 1550$, 2500, 3600, and 4750 for the four successive jets. As noted above, jet 3 (also our anticipated jet 5) is mirror-symmetric relative to the other jets, but the topological structure preserves its homologous character. For jets 1, 2, and 4, closed red field lines anchored on the left side of the system $(-y)$ have become open during the jet generation; prior to onset, the open red field lines were located on the right side. The strong twist on the newly reconnected and opened field lines is expelled toward the top boundary, as seen by the helical shape that they present in their upper parts. The untwisting jet is generated and driven by the nonlinear

fast Alfvén wave that carries away the magnetic helicity, as described previously in PAD09.

Simultaneously, the previously open red field lines on the right side ($+y$) have closed down. They reconnected with field lines located in the $-x$ domain (far half-space) on the left side ($-y$). The white field lines meanwhile have assumed the characteristic shape of a double inverted Y point à la Syrovatskii (1981). An intense current sheet is located centrally between the double Y points, similar to the spine/fan reconnection mode Priest & Pontin (2009) that also was observed in the simulations of Masson et al. (2009). This structure is reminiscent of the classical 2D picture of jets: white open field lines on the right are reconnecting with closed field lines to their left.

A "double-chambered vault" structure of closed loops develops below the jet, similar to that described by Moreno-Insertis et al. (2008). The left side would be equivalent to their "emerged chamber" while the "reconnected chamber" on the right in our simulation accumulates and compresses the reconnected plasma. The pressure and density are much higher in that region, and so would appear as bright points or loops in observations. The evolution obtained here also is similar to that described by Török et al. (2009): using our third jet as the comparison, the right panel of our Figure 5 is equivalent to the right panel of their Figure 3. Here, our open red field lines on the left are equivalent to their open red field lines, while our closed red and white field lines on the right can be associated with their blue field lines. The evolution of the field in the left and right panels of our Figure 6 is very similar to the corresponding evolution in the middle and right panels of Figure 3 of Török et al. (2009). In their phraseology, this phase corresponds to the formation of the first "half" of the anemone structure.

The fully 3D connectivity is much more complex than in the classical 2D picture. In Figure 6, left panel, going from left to right four separatrices are present, demarcating four successive transition between closed and open field. Recall that initially there were only two separatrices. On the left side, several red field lines are open (those actually responsible for the untwisting jet), bordered by both white and red neighboring field lines that are closed. Vertical current sheets are present along the separatrices between the open and closed field. This succession of closed and open field would not be possible in 2D, of course, and is therefore an intrinsically 3D property of the jet generation in our model. Although the starting footpoints of all of these field lines lie on a single line in the xy plane, their shapes are fully 3D, as are the connectivity domains. The 3D fan separatrix has been deformed in such a way that a 2D section seems to hold more connectivity domains. However, there are still only two simply connected connectivity domains in the system (closed and open): the open red field lines are behind (in the $-x$ domain) the closed white field lines (which are in the $+x$ domain). The footprint of the fan surface, which initially was circular, now

assumes the shape of a curled tadpole. The curled portion of the separatrix footprint rotates counterclockwise throughout the evolution of the system.

The four panels in the right column of Figure 6 correspond respectively to times $t = 1650$, 2550, 3700, and 4950, representing the end of the untwisting jet when the topology is much simplified. By comparison with the structure at time $t_{Ef,max}$ (right column of Figure 5), one observes a reflection symmetry relative to the central axis and spine line. For jets 1, 2, and 4 red field lines on the left side are now open while some white field lines on the right side are now closed (with mirror symmetry in the case of jet 3). Observationally, one would observe the jet on the left and a slightly shifted bright point or closed loop to its right (for jet 3, the bright point is to the left of the jet).

Figure 7 displays the topological structure during the relaxation phase following the jets. The four left panels correspond to times $t_{Ef,min}$ while in the right column the times are respectively $t = 2000$, 2800, 3950, and 5150. The quasi-homologous character of the jets is still evident. At $t_{Ef,min}$ we observe that the topology again is quite complex; indeed, it closely resembles the double inverted Y configuration previously described at the time of jet triggering (Fig. 6, left column), but mirror-reflected left to right. At this time, a perfectly homologous jet will have released the amount of energy that had been injected and stored since the preceding jet. The current sheet continues to rotate in response to the imposed footpoint motions. Field lines on the left side $(-y)$ have closed down while field lines on the right $(+y)$ have opened up. A substantial fraction of the field lines have now reconnected twice, while some – e.g., red field lines on the right side – have reconnected for a third time. These successive reconnections of particular field lines allow the system to release a large amount of energy and account for how efficiently the jet generation releases the stored free energy. Helicity is still transferred up and out of the system, but the amount of twist ejected is much reduced now. Closed field lines that are opening up now have a much smaller amount of helicity than before, since a substantial fraction of the accummulated helicity already has been ejected during previous reconnection events. This relaxation phase is comparable to the second stage of the anemone formation described by Török et al. (2009).

Finally, the right panels of Figure 7 present the final stage of magnetic reconfiguration associated with the impulsive jet generation. The quasi-homology of the configuration is again evident. At this time most of the helicity has been released. However, the connectivity of the system is different from that at the outset. Field lines near the fan separatrix have a different connectivity than in the initial state. Several red field lines at the right of the system $(+y)$ in jets 1, 2, and 4 are still open, while some white field lines on the left are closed. The topology is actually very similar to that observed at $t_{Ef,max}$ (compare the right column of Fig. 5 with the right column of Fig. 7). The principal difference is the amount of

helicity stored in the closed domain. At $t_{\mathrm{Ef,max}}$ the closed domain presented strongly twisted field lines, winding by a bit less than one turn around the central spine, which have since ejected their helicity along open field lines through the top of the simulation domain.

The subsequent evolution therefore is not impulsive but more quasi-steady: this is the relaxation phase during which the field-line connectivity slowly evolves back toward its initial configuration, as described in § 4.4 of PAD09. In the present study, unlike PAD09, new twist is simultaneously stored in the closed domain during the relaxation phase, due to the ongoing boundary motions. A current sheet is still present along the fan, mostly at the right side ($+y$) of the configuration (on the left for jet 3). The dissipation of the current is slow and quasi-steady, with the sheet remaining essentially fixed in place as in the classical picture with 2D reconnection (cf. § 4.2) and inducing a slow change in the connectivity. Comparing the final configuration of jets 2 and 3 with the initial structure of the following jets 3 and 4, respectively (cf. the right column of Fig. 7 with the left column of Fig. 5), one observes that the red field lines that were open have now closed and the system is in its initial topological state, ready for a new cycle of jet generation and relaxation.

4. DISCUSSION

4.1. Homology and Other Properties of the Magnetic Structure and Driving System

A first consequence of the 3D character of null-point reconnection that we want to stress is that individual field lines may reconnect several times during the generation of a single jet. Assuming that the relaxed state is similar to the initial state implies that all field lines that reconnected did so twice. We have seen that some field lines actually reconnect four times during one jet cycle, including several of the red field lines on the right side ($+y$) of the configuration. As is usual in 3D reconnection, there is not 2 by 2 field line reconnection but rather an exchange of magnetic flux through the separatrix surface Pontin et al. (e.g. 2004). In addition, a flux tube that reconnects multiple times does not interact with the same flux domain each time: flux is transferred successively between domains distributed all around the 3D separatrix. This behavior is also present in Török et al. (2009).

This character of 3D reconnection has important consequences: 2D models of reconnection at a null point between open and closed field lines predict that three UV ribbons will be formed at the intersection of the three separatrices connected to the solar surface (e.g., because of particles flowing along the reconnected field lines). With a 3D null point, only two ribbons normally would be expected to form: a circular ribbon corresponding to the

fan and a second ribbon related to the inner spine. However, when multiple reconnections occur, the prediction of the number of ribbons that may be induced is not straightforward. Ribbons will be formed along the separatrix, as the theory predicts, but only portions of it may brighten as discrete bundles of flux reconnect at the fan. In addition, the latter evolves so dynamically that it can induce a very large variety of possible distributions of the flare ribbons associated with the jet.

The present study shows that the 3D null point topology used in the present system clearly possesses a quasi-homologous behavior under the prescribed motions. All of the jets evolve through similar stages, presenting the same connectivity evolution as described in § 3.3. The system is not fully homologous from the outset, however, since the first and second jets present the same symmetry about the central axis and spine, which thereafter alternates mirror-symmetrically from jet to jet. We stress that this symmetry difference is most apparent when inspecting the connectivity of the field lines. All of the actual untwisting jets of plasma, on the other hand, will appear similar to each other. This is because the jet, comprised of the compressive part of the nonlinear Alfvén wave, follows the helical magnetic structure spiraling around its central axis along the open-field direction (see Fig. 4 of PAD09). This wave is axisymetrically invariant relative to the outer spine, so the four jets appear fully homologous.

The alternating left/right symmetry, however, will induce one difference in the apparent evolution of successive jets. As noted in § 4.3 of PAD09, the generation of the nonlinear wave results in an apparent drifting motion of the jet axis when observed from the side. This drifting motion is due to the rotation of the reconnection site. The direction of rotation here is counterclockwise (the opposite of the photospheric driving direction) for all of the untwisting jets, since they all eject positive magnetic helicity. The initial reconnection point for our jet 3 is diametrically opposite that for the other jets, thus the direction of its drifting motion (right to left) also is opposite that of the drift (left to right) observed for the other jets.

One interesting outcome of this study, therefore, is that the direction of the drifting motion of recurrent jets cannot be directly predicted even knowing the sign of the magnetic helicity injected, the driving direction, and the surface distribution of the field. In our four jets, we injected the same sign of helicity in exactly the same way, nonetheless we observed different drifting directions for different jets. We predict that for recurrent jets the direction of the drifting motion can change, even if the underlying magnetic system and the driving motion remain constant. Such behavior actually has been observed already: among the successive surges and jets studied by Chen et al. (2008), their jets 6 and 7 appeared to originate from different sides of the closed magnetic structure. Our model predicts that the

conclusions of Savcheva et al. (2009), that jets follow a Hale-like law, may change when only recurring jets are considered. More observational studies of recurring jets need to be performed to test our hypothesis.

The occurrence of jets on both sides of our configuration indicates that the global structure, specifically the orientation of the open field, is not the sole determining factor in the spatial location of the jet. Successive jets were generated with both identical left/right symmetry (jets 1-2) and opposite symmetry (jets 2-3 and 3-4). The system may be developing a memory of the symmetry of the previous jet as the initial conditions are forgotten, but it also is possible that the initiation point will vary rather chaotically from one jet to the next. Our results indicate that the distribution of electric current around the null point plays an important role in the onset of the energy-release process and in determining the direction of jet drift. These tentative conclusions are, of course, based on the simulation of just four successive jets at only one inclination of the open field with respect to the vertical. It is plausible that the global geometry of the system will influence the direction and shape of the jets on average. Our results thus should be considered as a starting point for future statistically significant parametric investigations.

One test that we performed addresses the influence of the driving velocity on the results. As mentioned in § 2, we ran another set of simulations in which the velocity magnitude was doubled. The kinetic and magnetic energy are presented in Figure 8, plotted for both runs as a function of the theoretical number of turns given to field lines rooted at unit radius from the central axis. The most important finding is that the doubled injection rate does not modify the quasi-homologous character of the system. As before, four quasi-homologous jets were generated, as indicated by the successive magnetic energy releases and the associated peaks in kinetic energy.

Some differences should be noted, however. The principal one is that the jets do not occur after the same amount of twist has been injected. More twist is injected in the fast run: 1.1 turns are imparted to the ($r = 1$) field line, while only 0.95 turns were applied during the slow run, by the onset time for the first jet. Higher twist also is observed to be necessary for all subsequent jets. While on average 0.98 turns were injected between successive jets in the fast run, only 0.87 were injected in the slow run. Another significant difference is the fact that in the fast run, the amplitude of the variations in magnetic and kinetic energies from jet to jet are larger than in the slow run. The increases in kinetic energy are less impulsive in the fast run, and several subsidiary peaks are observed. The kinetic energy also never returns as near to zero as it does with the slower driving speed.

A likely explanation for these differences is that, in the fast run, the driving velocity is simply too fast compared to the system response time. After any one jet has been generated,

the system does not have sufficient time to relax fully toward what would be its time-asymptotic state in the absence of additional driving. The imposed flows are too strong to allow the system to perform a complete cycle, and the result is a more chaotic behavior. Inspecting the connectivity in the fast run reveals that the relaxation phases do not proceed to completion, and the system is constantly reconnecting although at different rates. This is why significant kinetic energy is always present in the system in the fast run.

Similarly, the larger number of turns at the energy maxima do not accurately correspond to the actual starting point of the jets. For the fast run, the instant at which the connectivity most closely resembles that assumed by the slow run at $t_{\text{Ef,max}}$ (right column of Fig. 5) in fact corresponds to slightly more than 0.9 turns. Therefore, from the point of view of field-line connectivity, the slow and fast jets occur at the same moment. In the fast run, however, a significant amount of additional energy is injected during the initial phase of the jet, thereby shifting to a later time the instant at which the maximum free energy is reached. Similarly, additional helicity is injected while the system is in the process of opening up, so that larger amounts of twist are both ejected and also stored within the closed domain. Thus, the minimum energies also are higher in the fast run than in the slow run.

Even in the fast run, the quasi-homologous property of the jets is preserved, although the higher energy injection rate clearly modifies the detailed dynamics of the system. In order to observe unambiguously the homologous character, the system must have time to relax substantially between jets. Both driving velocities used here ($\sim 2.5\%$ and $\sim 1.2\%$ of the coronal Alfvén velocity for the fast and slow runs, respectively) exceed by at least by an order of magnitude the velocities typically observed at the photosphere. The true solar forcing therefore is likely gradual enough for the null-point topology to relax fully and reconfigure itself. In numerical simulations, time and resource constraints demand the use of relatively fast driving velocities. One lesson imparted by this experiment is that the forcing nonetheless must remain slow enough to allow at least partial global relaxation to occur, thereby revealing the homologous character of the evolution.

Overall, the homologous property is a particularly stringent constraint on jet models. The homology may result from the properties of the driving mechanism, of the magnetic system, or of a combination of both. Given the diversity of proposed forcing mechanisms – e.g. flux cancellation, flux emergence, and shearing motions – it is unlikely that the forcing itself can explain the homologous property. A magnetic structure whose reaction is completely insensitive to the driving mechanism could possess a homologous character, but this would imply stringent constraints on the class of allowed structures. Since the coronal energization is achieved through the photospheric boundary evolution, the forcing mechanism is likely to influence strongly the dynamics of the magnetic system even though the response is likely

to be highly nonlinear, as demonstrated by the present study.

The fully 3D system studied here is the second that presents a reformation of the source region and a succession of eruptive events with a homologous property. As in DeVore & Antiochos (2008), this evolution of the system is enabled by two characteristics of the driving forcing: the preservation of the radial magnetic flux distribution at the coronal base and the moderate but continuous twisting stress applied. Arguments detailing the numerical and observational rationale for these boundary-driven motions have been presented at length in DeVore & Antiochos (2008) and PAD09. Because magnetic flux cancellation also is commonly observed in conjunction with jets (e.g. Chifor et al. 2008a,b), further studies usefully could address the generation of homologous jets in a 3D null-point topology subject to such stresses.

As in the system presented in DeVore & Antiochos (2008), our experiment also shows that the homologous property of the system is inherently linked to its capacity to relax to some quasi-potential state. Only then can the system be susceptible to subsequent homologous recurring jets. It is worth mentioning that both configurations exhibiting such homologous behavior are based on the topology of a 3D null point. This structure may be more generally linked with a homologous property of other phenomena, since it seems to be a property of the 3D null-point system that it strives to reach a state approximating its initial potential field. We suggest that any imposed field evolution that allows the 3D null-point topology to reform to nearly its pre-event state will enable the generation of successive quasi-homologous events.

Interestingly, a 3D null-point topology also results from the interaction of an emerging twisted flux tube with a large-scale field (cf. Fig. 5 of Török et al. 2009). In that simulation, the final 3D null is strongly asymmetric, with significant twist being stored in its vicinity. Overall the topology and connectivity are quite similar to the initial configuration of the present study. Our simulations combined with those of Török et al. (2009) therefore can draw a complete picture of the jet generation process in coronal holes. Even though in the simulation of Török et al. (2009) the field is closed, strictly speaking, at the scale of the emerging flux tube, the surrounding field is similar to an open-flux region having relatively uniform and vertical magnetic field. Török et al. (2009) thus can explain how a fully 3D null-point topological structure can be formed following the emergence of a twisted flux tube into an open field. The emergence not only triggers an untwisting jet similar to that described here and in PAD09, but also forms a fully 3D null-point topology. It is straightforward to imagine that the ongoing injection of twist and energy into that system would result naturally in the generation of recurring jets as obtained in this study.

4.2. Presence of Two Reconnection Regimes

The evolution of the system described here presents two very different reconnection regimes. The first, which coincides with the generation of the untwisting jet, is extremely dynamic. In the second, which is realized during the relaxation phase, the evolution of the system is more quasi-steady.

The existence of these two regimes is mainly observed through the dynamical evolution of the current sheet. Some facets of the relaxation phase have been described in PAD09. A thin current sheet located along the fan separatrix is present during the later phase of the homologous jet cycle, much as in Figure 12 of PAD09. We observe that the inner and outer spines have been displaced relative to each other along the fan. As noted by Masson et al. (2009), the most intense currents are located between the sheared spine lines, following the topology described by Antiochos (1996). Reconnection proceeds so as to bring the two spines back into alignment through a slowly evolving, quasi-static state. During this evolution, the current sheet remains relatively stable in intensity and location.

Interestingly, this regime occurs not only after a jet is generated, but also can precede it. Indeed, as noted in § 3.1, even before the onset of the first jet some plasma is accelerated. This is due to the presence of a thin current sheet along the fan separatrix (see Fig. 9). This current sheet intensifies in response to the boundary driving motions. As the system evolves, the magnetic pressure increases in the closed domain, exerting a force on the null point itself. In a way similar to Masson et al. (2009), the closed field bulges in a direction almost perpendicular to the fan, inducing a compression of the 3D null point. Since the system is asymmetric due to the inclination of the background field, the forces applied to the inner and outer spine are unbalanced. This leads to a shear displacement of the spines along the fan surface, so that the initial alignment (Fig. 1) gives way to a state in which the inner and outer spines are well separated (Fig. 9).

The current sheet strengthening between the sheared spines eventually suffers magnetic reconnection. We note that the prescribed velocity field is almost zero near the center of the embedded magnetic polarity, so that field lines below and adjacent to the fan surface are only very moderately sheared. Thus, the current sheet remains initially mostly in the yz plane. As the twist accumulates, however, an additional azimuthal shear develops, displacing and eventually deforming the null point. The current sheet then extends out of the yz plane and spreads in the $-x$ direction, following the clockwise deformation of the field lines (see Fig. 9). This gradual rotation, of slightly more than $\pi/4$ over 700 time units, is slow relative to the evolution of the rest of the system.

The thin current sheet induces some magnetic reconnection, changing the connectivity

of some field lines close to the fan surface (cf. the evolution of the pink field line in Fig. 9). Field lines located increasingly far from the initial fan surface successively reconnect. However, the amount of flux reconnected remains extremely limited in the present simulation relative to the total flux in the closed domain. The size and length of the current sheet increase slowly and smoothly in time as the boundary driving motion accelerates during the initial phase. The rate of reconnection remains limited and is not sufficient to compensate the forcing; therefore the magnetic free energy steadily increases. Furthermore, this quasi-steady reconnection does not penetrate deeply into the closed flux region, because the reconnection acts to release the twist, thereby, weakening the current sheet. It is only through the resistive kink instability, which the feedback between the reconnection and the ideal evolution, that the current sheet can penetrate deeply into the stressed field region.

The evolution of the current sheet during the jet generation contrasts sharply with the quasi-steady currents during the non-jetting phse. As presented in Figure 10, the jet current sheet differs morphologically and dynamically from that prior to and following the jet. First, the jet current sheet is much larger than its quasi-steady counterparts. In the relaxation phase the current sheet has a relatively small extension, while the jet current sheet covers a very large area. Also, while the quasi-steady current sheet is approximately planar, the jet current sheet has a pronounced 3D helical structure. The helix curls around up to about one full turn. Within the thin sheet, the currents are not aligned with the magnetic field but instead roughly follow the helical shape of the sheet. Visual inspection reveals that the magnetic field lines tend to be nearly perpendicular on opposite sides of the current sheet. Following Ampère's law, the currents are directed along the bisector of the magnetic field lines. Consequently, the pitch of the current sheet is opposite in sign to that of the field lines, as can be seen in Figure 10.

The fully 3D shape of the current sheet is one fundamental difference with the classical 2D picture of jet reconnection. Field lines can (and do!) reconnect at diverse points simultaneously. The very large surface area of the current sheet enables reconnection to occur at numerous locations, thereby supporting a high reconnection rate. This accounts, in part, for the large amount of energy released during the jet generation.

A second important difference with the classical 2D picture is the highly dynamic evolution of the current sheet. As shown in Figure 10, the current sheet undergoes a 3D rotation around the closed flux domain. For example, in the figure, at time $t = 1450$ the top of the helical current sheet is located toward $-y$, at $t = 1550$ toward $+x$, and then toward $+y$ and $-x$ at $t = 1650$ and 1800, respectively. In about 500 time units, the current sheet rotates through one turn in the 3D space. This rotation of the current sheet coincides with a rotation of the region of weak magnetic fields. A similar rotation of the null point was

noted by Török et al. (2009) during the generation of their twisting jet.

This rotation of the current sheet supports the reconnection of a large amount of magnetic flux. Cumulatively, the rotating current sheet spans a sizeable fraction of the domain, so that reconnection becomes possible over a large area. This explains why so much of the twisted magnetic flux can reconnect, releasing the twist into the open domain. Newly reconnected field lines have a large amount of twist concentrated in their lower parts. A nonlinear Alfvén wave propagates the twist up and outward, thereby drawing the field line away from the reconnection site. This allows field lines located slightly to the side of the reconnected ones to come into close contact within the reconnection region, inducing a rotation of the current sheet. This process is the essence of a resistive-kink type mode. Reconnection produces force imbalances in the system that drive motions, which strengthgen the current sheet, resulting in even more reconnection.

This jet-reconnection regime, involving a fully 3D current sheet developing and rotating quickly in the 3D space, is fundamentally different from the 2D picture of reconnection wherein the current sheet moves only slowly due to the evolution of the separatrices. The complex interaction between reconnected field lines and electric current allows a very efficient energy release differing markedly from the quasi-steady mode described earlier. The impulsive launching of the untwisting jet and nonlinear Alvén wave is likely to be triggered by an instability. Török et al. (2009) noted that the perturbation of their system at jet onset, which yielded an increase of the reconnection rate, occurred when a twist of 1.5 turns had been induced in the flux rope. They cited ideal kink instability as a possible mechanism for onset. PAD09 and Rachmeler et al. (2010) noted that a threshold of about 1.4 turns was required for the kink instability to occur and the jet to be triggered. In the present study, our homologous jets are initiated after a smaller, but roughly fixed, amount of twist has been injected (0.85 ± 0.1, see § 3.2). These different values obtained for different inclination angles θ of the open field indicate that the exact criterion for fast reconnection onset is sensitive to the system details, but the basic result is robust. Photospheric twisting in the embedded bipole topology of PAD09 will eventually lead to reconnection bursts and accompanying jets.

4.3. Relationship Between Jets and Plumes

An important outcome of the existence of these two regimes of reconnection is that the observed link between coronal jets and plumes might be explained in a simple way. Unlike collimated jets, plumes are hazy, diffuse structures within coronal holes (e.g. Deforest et al. 1997, 2001b; Wilhelm 2006; Wang & Muglach 2007; Curdt et al. 2008) that have a lifetime (0.5-2 days Deforest et al. 1997, 2001a) an order of magnitude longer than impulsive jets.

As pointed by Raouafi et al. (2008), despite their quite different appearance and duration, jets and plumes share a number of common properties that suggest related generation processes. Both arise in similar magnetic structures: like jets, plumes trace the open field lines of coronal holes (e.g. Young et al. 1999; Deforest et al. 2001b) and also root in regions of enhanced magnetic flux exhibiting mixed polarities (Wang et al. 1997). Improved temporal and spatial resolution of recent observational studies have revealed even closer relationships between jets and plumes. Jet-like EUV events frequently are observed within plumes (e.g. Wang et al. 2008; Raouafi 2009). Raouafi et al. (2008) noted that plume emission is enhanced following jet eruptions from the base of the plume, and found that more than 90% of their X-ray jets were related to a plume. In 70% of such cases, plume haze appears from a few minutes to a few tens of minutes following the triggering of the jet. Raouafi (2009) also reported two events in which the formation of an impulsive collimated X-ray jet, its morphological transformation into a larger hazy structure, and the subsequent appearance of a typical EUV plume could all be related directly.

Raouafi et al. (2008) concluded that jets are likely to play a key role in the formation of plumes. As is the case for jets, the most broadly accepted mechanism for plumes involves reconnection between open and closed magnetic fields (Wang 1998). This reconnection induces enhanced heating of plasma at the base of the plume, accounting for the higher density of the plume material (Wang 1994). If indeed reconnection is responsible for both jets and plumes, how can one explain their disparate time scales? Raouafi (2009) postulated that coronal jets occur due to impulsive reconnection between the closed and ambient open coronal fields, while plumes result from the residual heating associated with gradual reconnection. Our present simulations and analysis reveal the existence of two distinct regimes of reconnection associated with jet generation, thereby strongly supporting the suggestion by Raouafi (2009) and accounting for the observed relationship between jets and plumes.

Our simulation model relies on numerical dissipation rather than an explicit resistive term in the inductions equation, and so does not capture the Joule heating that occurs at the reconnection current sheet. Thus, we are unable to calculate the detailed thermodynamic evolution of the plasma in the quasi-steady regime. Although we cannot compare our simulation results quantitatively with actual plume observations, it is clear that quasi-steady reconnection should provide a ready heat source for plumes. The link between the two reconnection regimes also simply explains the common properties of jets and plumes and their observed spatial and temporal relationships.

While the jet duration is relatively short, averaging 375 time units, the interval of quasi-steady reconnection is significantly more extended. In our "slow" simulation, the relaxation phase lasts an average of 710 time units, twice the duration of the jet. However, this is only

a lower limit since, as discussed in § 4.1, our simulation assumes a driving speed much faster than that on the Sun. In PAD09, we imposed no driving motions after the onset of the jet, and the relaxation phase continued for more than three times the jet duration before the simulation was halted. At that point, the current sheet was still present and quasi-steady reconnection was continuing. The 3D impulsive and 2D quasi-steady reconnection modes observed here thus are likely to be compatible with the observed, disparate time scales of jets and plumes, respectively. Further detailed investigation of the mechanisms is in order, of course, but we believe that the fundamental process described in this paper is a promising explanation for the jet/plume link postulated by Raouafi (2009).

5. SUMMARY

The present simulations extend the numerical investigations of the jet model pursued first by Pariat et al. (2009, PAD09) and continued in Patsourakos et al. (2008) and Rachmeler et al. (2010). The simulations were performed with the state-of-the-art ARMS model, a fully 3D parallel MHD solver using adaptive mesh refinement. This code enables us to simulate the accumulation of the magnetic free energy underlying the jets, and its impulsive liberation and transformation thereafter through magnetic reconnection. We have followed the evolution of the energies and the connectivity of the magnetic field in a quasi-ideal medium that emulates the solar corona.

In PAD09 we presented a model for jets based on interchange reconnection between open and closed magnetic fields, which generates an impulsive, nonlinear Alfvén wave that ejects along open field lines most of the helicity previously stored in the closed domain. The experiments pursued here differ from the original presented in PAD09 in two main ways (cf. § 2). First, the forcing boundary motions now have been applied continuously to the magnetic system, which contains both open- and closed-connectivity domains associated with a 3D null-point topology. Second, the initial axisymmetry of PAD09's magnetic configuration, which inhibited reconnection between the closed and open fields, has been broken by tilting the large-scale background field with respect to the vertical. The main results of our analysis can be summarized as follows:

1. The 3D null-point topological system driven continuously by twisting motions naturally produces successive jets (cf. § 3). Our model therefore can account for recurring jets originating in a single magnetic source, as is commonly observed in the solar corona (cf. § 1).

2. Each recurring jet is generated once a threshold amount of free energy and helicity has

been injected since the cessation of the previous jet (cf. § 3.2). The necessary twist is similar for all four of our jets, $\sim 0.85 \pm 0.1$ turns. This value seems not to be influenced by the driving velocity. However, it differs substantially from the much larger threshold value of ~ 1.4 turns found in our previous simulation with an axisymmetric magnetic field. Clearly, the magnetic structure influences strongly the trigger threshold for the jets.

3. The 3D reconnection at the null point is extremely dynamic, and field lines in its vicinity generally reconnect several times. The number of UV ribbons that eventually will be formed during the jet generation cannot be predicted straightforwardly as in the 2D model.

4. The successive jets are quasi-homologous to each other (cf. § 3.3), i.e. they are of comparable size, are collimated in the same direction, and present the same helical structure. The homology seems to be a natural consequence of the 3D null-point system, which through reconnection can reform the topology of its initial state; this was described previously by DeVore & Antiochos (2008) for confined filament eruptions.

5. A left/right reflection symmetry appears in the detailed connectivity evolution of the jet magnetic structure (cf. § 3.3). While this symmetry does not change the jet morphology and direction, it nonetheless modifies its apparent dynamics by changing the direction of the drifting motion of the jet axis (cf. § 4.1). Our simulation predicts that recurring jets may drift in either direction when viewed from the side. The geometry and helicity of the magnetic configuration are not the sole factors in determining the direction of drift of the jet axis; the detailed structure and evolution of the jet current sheet also are very important.

6. The generation of the recurring jets is divided into two distinct phases (cf. § 3.1): the energy-storage phase, in which free magnetic energy accumulates prior to jet onset and during the relaxation following jet cessation; and the energy-release phase, in which the stored free energy is impulsively liberated and the untwisting magnetic jet is launched.

7. These two phases are associated with two very distinct regimes of reconnection (cf. § 4.2). The jet generation involves an extended thin 3D helical current sheet that dynamically rotates in the space between the closed and open domains, and across which magnetic flux can reconnect over a very large surface area. This impulsive and extremely dynamic mode of 3D reconnection differs substantially from the classical picture of 2D reconnection. The latter process is the dominant regime during the energy build-up and relaxation phases of the jet evolution, however. A quasi-steady current sheet forms between the sheared spine lines, spatially localized along the fan

surface. Reconnection across this sheet gradually restores the initial connectivity of the magnetic field, setting the stage for the generation of the next jet in the sequence.

8. The quasi-steady regime also appears prior to the jet generation as a direct consequence of the forcing applied to the 3D null point in response to the imposed boundary motions (cf. § 4.2). This behavior was not observed in PAD09 and is a consequence of the broken axisymmetry of the initial magnetic configuration, which allows reconnection to occur much earlier. The nature of this current sheet and its ongoing reconnection are distinctly different from those responsible for the jets. While plasma surely is accelerated away from the reconnection site, the reconnection mechanism and rate are very different from the impulsive 3D mode of reconnection occurring in conjunction with the jet triggering.

9. Another important outcome of our study is a plausible link between polar plumes and jets (cf. § 4.3). The existence of two distinct regimes of reconnection in a single geometry supports a postulate by Raouafi (2009) that coronal jets and plumes are closely related events differing principally by the nature of the reconnection that takes place. We suggest that coronal jets are the direct consequence of an impulsive 3D reconnection mode, triggered by an instability whose precise nature remains to be determined. Plumes result from the quasi-steady 2D reconnection mode associated with the relaxation phase following jet cessation. We predict that long-lived plumes should be fed regularly by recurring jets, and that the latter are likely to be seen more frequently within plumes as temporal and spatial resolution of solar instruments improve.

REFERENCES

Alexander, D. & Fletcher, L. 1999, Solar Physics, 190, 167, (c) 1999: Kluwer Academic Publishers

Antiochos, S. K. 1996, Solar drivers of the interplanetary and terrestrial disturbances. Astronomical Society of the Pacific Conference Series, 95, 1

Archontis, V., Gontikakis, C., & Tsinganos, K. 2010, Astronomy and Astrophysics, in press

Archontis, V., Hood, A. W., & Brady, C. 2007, A&A, 466, 367

Archontis, V., Moreno-Insertis, F., Galsgaard, K., Hood, A., & O'shea, E. 2004, A&A, 426, 1047

Archontis, V., Moreno-Insertis, F., Galsgaard, K., & Hood, A. W. 2005, The Astrophysical Journal, 635, 1299

Asai, A., Ishii, T. T., & Kurokawa, H. 2001, The Astrophysical Journal, 555, L65, (c) 2001: The American Astronomical Society

Canfield, R. C., Reardon, K. P., Leka, K. D., Shibata, K., Yokoyama, T., & Shimojo, M. 1996, Astrophysical Journal v.464, 464, 1016

Chae, J., Qiu, J., Wang, H., & Goode, P. R. 1999, The Astrophysical Journal, 513, L75, (c) 1999: The American Astronomical Society

Chen, H. D., Jiang, Y. C., & Ma, S. L. 2008, A&A, 478, 907

Chifor, C., Isobe, H., Mason, H. E., Hannah, I. G., Young, P. R., Zanna, G. D., Krucker, S., Ichimoto, K., Katsukawa, Y., & Yokoyama, T. 2008a, A&A, 491, 279

Chifor, C., Young, P. R., Isobe, H., Mason, H. E., Tripathi, D., Hara, H., & Yokoyama, T. 2008b, A&A, 481, L57

Cirtain, J. W., Golub, L., Lundquist, L. L., Ballegooijen, A. V., Savcheva, A., Shimojo, M., de Luca, E. E., Tsuneta, S., Sakao, T., Reeves, K., Weber, M. A., Kano, R., Narukage, N., & Shibata, K. 2007, Science, 318, 1580

Curdt, W., Wilhelm, K., Feng, L., & Kamio, S. 2008, A&A, 481, L61

Deforest, C. E., Hoeksema, J. T., Gurman, J. B., Thompson, B. J., Plunkett, S. P., Howard, R., Harrison, R. C., & Hassler, D. M. 1997, Solar Physics, 175, 393, (c) 1997: Kluwer Academic Publishers

Deforest, C. E. & Kankelborg, C. C. 2007, Journal of Atmospheric and Solar-Terrestrial Physics, 69, 116, elsevier Ltd

Deforest, C. E., Lamy, P. L., & Llebaria, A. 2001a, The Astrophysical Journal, 560, 490, (c) 2001: The American Astronomical Society

Deforest, C. E., Plunkett, S. P., & Andrews, M. D. 2001b, The Astrophysical Journal, 546, 569, (c) 2001: The American Astronomical Society

DeVore, C. R. 1991, Journal of Computational Physics (ISSN 0021-9991), 92, 142

DeVore, C. R. & Antiochos, S. K. 2008, ApJ, 680, 740

Fletcher, L., Metcalf, T. R., Alexander, D., Brown, D. S., & Ryder, L. A. 2001, The Astrophysical Journal, 554, 451

Gontikakis, C., Archontis, V., & Tsinganos, K. 2009, Astronomy and Astrophysics, 506, L45

Gu, X. M., Lin, J., Li, K. J., Xuan, J. Y., Luan, T., & Li, Z. K. 1994, Astronomy and Astrophysics (ISSN 0004-6361), 282, 240

Gurman, J. B., Thompson, B. J., Newmark, J. A., & Deforest, C. E. 1998, ASP Conf. Ser. 154, 154, 329

Harrison, R. A., Bryans, P., & Bingham, R. 2001, A&A, 379, 324

Jiang, Y. C., Chen, H. D., Li, K. J., Shen, Y. D., & Yang, L. H. 2007, A&A, 469, 331

Jibben, P. & Canfield, R. C. 2004, The Astrophysical Journal, 610, 1129, (c) 2004: The American Astronomical Society

Kaiser, M. L., Kucera, T. A., Davila, J. M., Cyr, O. C. S., Guhathakurta, M., & Christian, E. 2008, Space Sci Rev, 136, 5, (c) 2008: Springer Science+Business Media B.V.

Kamio, S., Hara, H., Watanabe, T., Matsuzaki, K., Shibata, K., Culhane, L., & Warren, H. P. 2007, Publications of the Astronomical Society of Japan, 59, 757, (c) 2007: Astronomical Society of Japan

Kim, Y.-H., Kim, K.-S., & Jang, M. 2001, Solar Physics, 203, 371, (c) 2001: Kluwer Academic Publishers

Liu, Y. & Kurokawa, H. 2004, The Astrophysical Journal, 610, 1136, (c) 2004: The American Astronomical Society

MacNeice, P., Olson, K. M., Mobarry, C., de Fainchtein, R., & Packer, C. 2000, Computer Physics Communications, 126, 330

Masson, S., Pariat, E., Aulanier, G., & Schrijver, C. J. 2009, The Astrophysical Journal, 700, 559

Miyagoshi, T. & Yokoyama, T. 2004, The Astrophysical Journal, 614, 1042

Moreno-Insertis, F., Galsgaard, K., & Ugarte-Urra, I. 2008, The Astrophysical Journal, 673, L211

Nishizuka, N., Shimizu, T., Nakamura, T., Otsuji, K., Okamoto, T. J., Katsukawa, Y., & Shibata, K. 2008, The Astrophysical Journal, 683, L83, (c) 2008: The American Astronomical Society

Nistico, G., Bothmer, V., Patsourakos, S., & Zimbardo, G. 2009, eprint arXiv, 0906, 4407

Pariat, E., Antiochos, S. K., & DeVore, C. R. 2009, ApJ, 691, 61

Pariat, E., Démoulin, P., & Berger, M. A. 2005, A&A, 439, 1191

Patsourakos, S., Pariat, E., Vourlidas, A., Antiochos, S. K., & Wuelser, J. P. 2008, ApJ, 680, L73, (c) 2008: The American Astronomical Society

Pontieu, B. D., Mcintosh, S. W., Carlsson, M., Hansteen, V. H., Tarbell, T. D., Schrijver, C. J., Title, A. M., Shine, R. A., Tsuneta, S., Katsukawa, Y., Ichimoto, K., Suematsu, Y., Shimizu, T., & Nagata, S. 2007, Science, 318, 1574

Pontin, D. I. & Galsgaard, K. 2007, Journal of Geophysical Research, 112, 03103

Pontin, D. I., Hornig, G., & Priest, E. R. 2004, Geophysical and Astrophysical Fluid Dynamics, 98, 407

Priest, E. R. & Pontin, D. I. 2009, Physics of Plasmas, 16, 2101, (c) 2009: American Institute of Physics

Rachmeler, L. A., Pariat, E., Deforest, C. E., & Antiochos, S. K. 2010, The Astrophysical Journal, submitted

Raouafi, N.-E. 2009, Proceedings of the Hinode 2 meeting, 0902, 591

Raouafi, N.-E., Petrie, G. J. D., Norton, A. A., Henney, C. J., & Solanki, S. K. 2008, The Astrophysical Journal, 682, L137, (c) 2008: The American Astronomical Society

Savcheva, A., Cirtain, J., Deluca, E. E., Lundquist, L. L., Golub, L., Weber, M., Shimojo, M., Shibasaki, K., Sakao, T., Narukage, N., Tsuneta, S., & Kano, R. 2007, Publications of the Astronomical Society of Japan, 59, 771

Savcheva, A., Cirtain, J. W., Deluca, E. E., & Golub, L. 2009, The Astrophysical Journal Letters, 702, L32

Schmahl, E. J. 1981, Solar Physics, 69, 135, a&AA ID. AAA029.073.007

Schmieder, B., Shibata, K., van Driel-Gesztelyi, L., & Freeland, S. 1995, Solar Physics (ISSN 0038-0938), 156, 245

Shibata, K., Ishido, Y., Acton, L. W., Strong, K. T., Hirayama, T., Uchida, Y., McAllister, A. H., Matsumoto, R., Tsuneta, S., Shimizu, T., Hara, H., Sakurai, T., Ichimoto, K., Nishino, Y., & Ogawara, Y. 1992, PASJ: Publications of the Astronomical Society of Japan (ISSN 0004-6264), 44, L173

Shibata, K., Nakamura, T., Matsumoto, T., Otsuji, K., Okamoto, T. J., Nishizuka, N., Kawate, T., Watanabe, H., Nagata, S., Ueno, S., Kitai, R., Nozawa, S., Tsuneta, S., Suematsu, Y., Ichimoto, K., Shimizu, T., Katsukawa, Y., Tarbell, T. D., Berger, T. E., Lites, B. W., Shine, R. A., & Title, A. M. 2007, Science, 318, 1591

Shibata, K., Nitta, N., Strong, K. T., Matsumoto, R., Yokoyama, T., Hirayama, T., Hudson, H., & Ogawara, Y. 1994, The Astrophysical Journal, 431, L51

Shibata, K., Shimojo, M., Yokoyama, T., & Ohyama, M. 1997, Magnetic Reconnection in the Solar Atmosphere. ASP Conference Series; Vol. 111; 1997; ed. R. D. Bentley and J. T. Mariska (1997), 111, 29

Shibata, K. & Uchida, Y. 1985, Astronomical Society of Japan, 37, 31

—. 1986, Solar Physics (ISSN 0038-0938), 103, 299

Shimojo, M., Hashimoto, S., Shibata, K., Hirayama, T., Hudson, H. S., & Acton, L. W. 1996, Publ. of the Astronomical Society of Japan, 48, 123

Shimojo, M. & Shibata, K. 2000, The Astrophysical Journal, 542, 1100

Shimojo, M., Shibata, K., & Harvey, K. L. 1998, Solar Physics, 178, 379

Syrovatskii, S. I. 1981, In: Annual review of astronomy and astrophysics. Volume 19. (A82-11551 02-90) Palo Alto, 19, 163

Török, T., Aulanier, G., Schmieder, B., Reeves, K. K., & Golub, L. 2009, A&A

Tziotziou, K., Tsiropoula, G., & Mein, P. 2003, A&A, 402, 361

Wang, A. H., Wu, S. T., Liu, Y., & Hathaway, D. 2008, ApJ, 674, L57

Wang, Y.-M. 1994, Astrophysical Journal, 435, L153

Wang, Y. M. 1998, Astrophysical Journal Letters v.501, 501, L145

Wang, Y.-M. & Muglach, K. 2007, The Astrophysical Journal, 666, 1284

Wang, Y.-M., Pick, M., & Mason, G. M. 2006, The Astrophysical Journal, 639, 495, (c) 2006: The American Astronomical Society

Wang, Y.-M. & Sheeley, N. R. 2002, The Astrophysical Journal, 575, 542

Wang, Y.-M., Sheeley, N. R., Dere, K. P., Duffin, R. T., Howard, R. A., Michels, D. J., Moses, J. D., Harvey, J. W., Branston, D. D., Delaboudiniere, J.-P., Artzner, G. E., Hochedez, J. F., Defise, J. M., Catura, R. C., Lemen, J. R., Gurman, J. B., Neupert, W. M., Newmark, J., Thompson, B., & Maucherat, A. 1997, Astrophysical Journal Letters v.484, 484, L75, (c) 1997: The American Astronomical Society

Wang, Y.-M., Sheeley, N. R., Socker, D. G., Howard, R. A., Brueckner, G. E., Michels, D. J., Moses, D., Cyr, O. C. S., Llebaria, A., & Delaboudinière, J.-P. 1998, The Astrophysical Journal, 508, 899

Wilhelm, K. 2006, A&A, 455, 697

Yamauchi, Y., Moore, R. L., Suess, S. T., Wang, H., & Sakurai, T. 2004, The Astrophysical Journal, 605, 511

Yokoyama, T. & Shibata, K. 1995, Nature, 375, 42

—. 1996, Publ. of the Astronomical Society of Japan, 48, 353

Young, P. R., Klimchuk, J. A., & Mason, H. E. 1999, A&A, 350, 286

Table 1. Energy and time data for the recurring jets.

Jet	Energy					Time			
	$E_{\mathrm{f,max}}$	$E_{\mathrm{f,min}}$	$\Delta_R E_{\mathrm{f}}$	$\Delta_S E_{\mathrm{f}}$	ΔE_{kin}	$t_{\mathrm{Ef,max}}$	$t_{\mathrm{Ef,min}}$	Δt_{max}	Δt_{min}
$n°1$	32	17	-15	—	1.6	1440	1750	—	—
$n°2$	28	12	-16	11	1.6	2390	2700	950	950
$n°3$	27	15	-12	15	2.1	3430	3790	1040	1090
$n°4$	24	14	-10	9	1.2	4550	5070	1120	1280
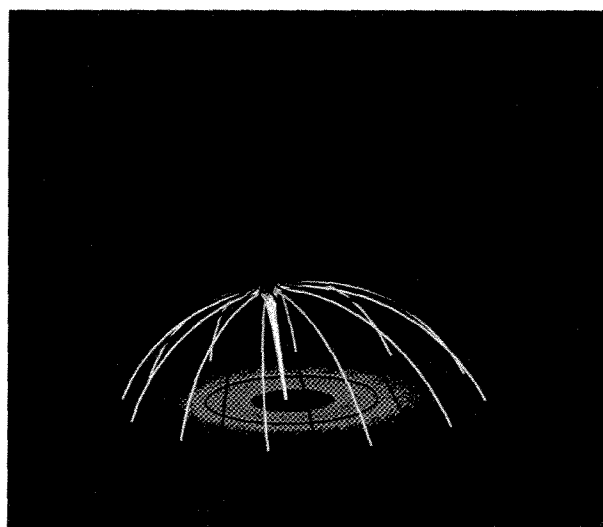
Fig. 1.— 3D view of the initial magnetic configuration. The distribution of the magnetic field intensity $|\mathbf{B}|$ at the $\{z = 0\}$ bottom (photospheric) plane is color-shaded: [purple; blue; cyan; green; yellow; red] correspond to field intensities equal to [12.5; 10; 7.5; 5; 2.5; 0], respectively. The black circle on this plane represents the polarity inversion line. Field lines belonging to the inner connectivity (closed) domain are plotted in white, while those belonging to the outer connectivity (open) domain are displayed in blue. The location of the 3D null point is illustrated by a red isosurface.
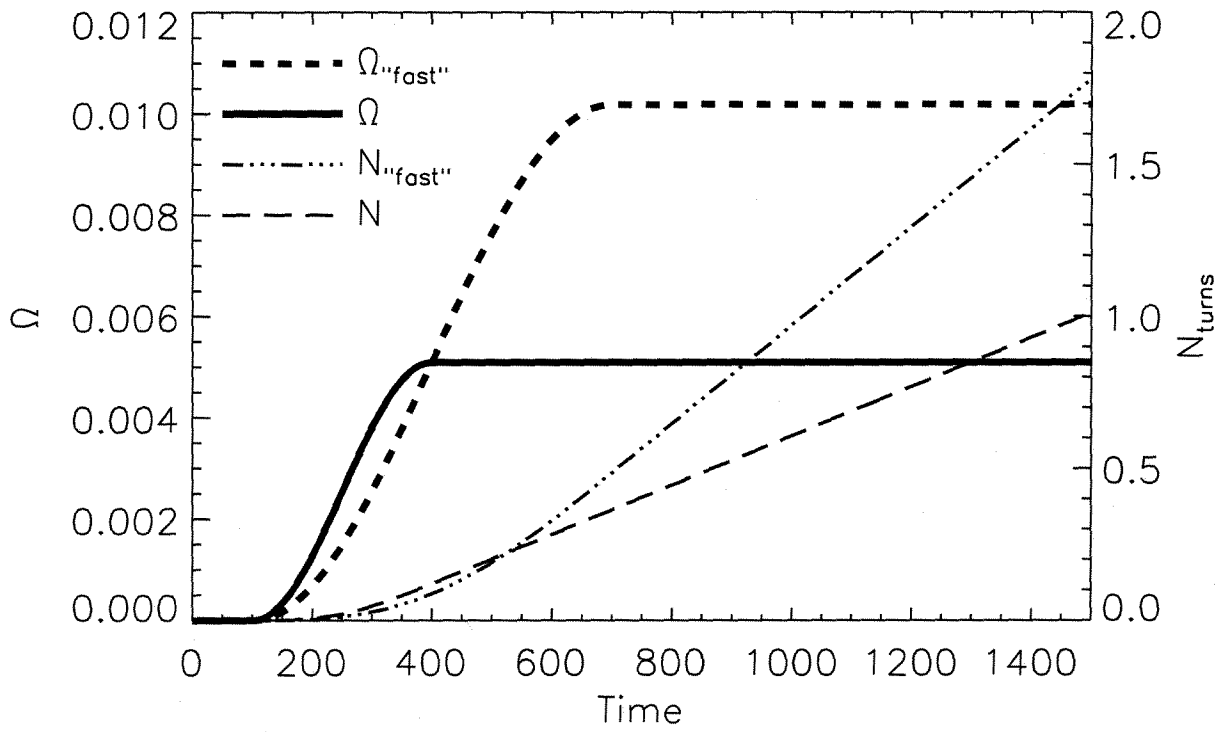
Fig. 2.— Evolution of the rotation rate at radius $r = 1$ and the corresponding number of turns given to the field lines for each run.
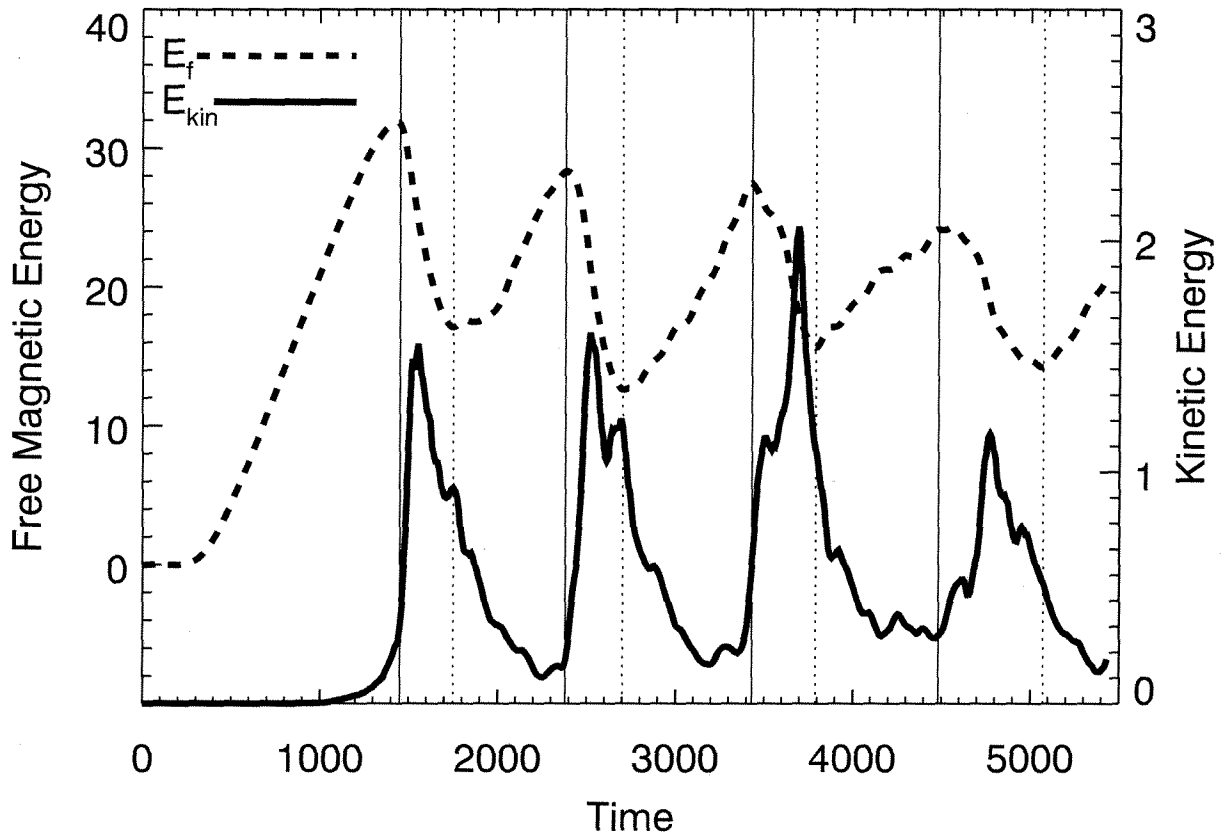
Fig. 3.— Evolution of the kinetic (*solid line*) and free magnetic (*dashed line*) energies during the simulation. The solid vertical lines correspond to times $t_{Ef,max}$ of maxima of the free energy; the dotted vertical lines indicate times $t_{Ef,min}$ of minima.
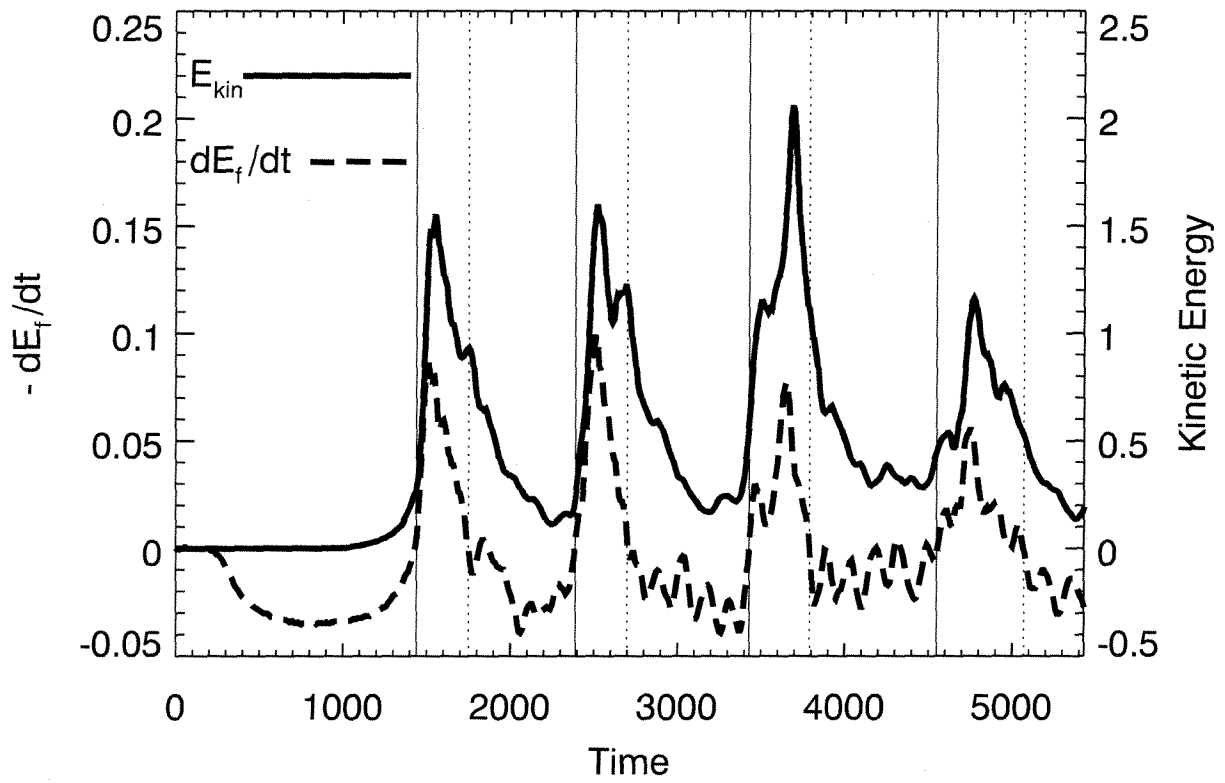
Fig. 4.— Evolution of the kinetic energy (*solid line*) and the derivative of the free magnetic energy (*dashed line*).
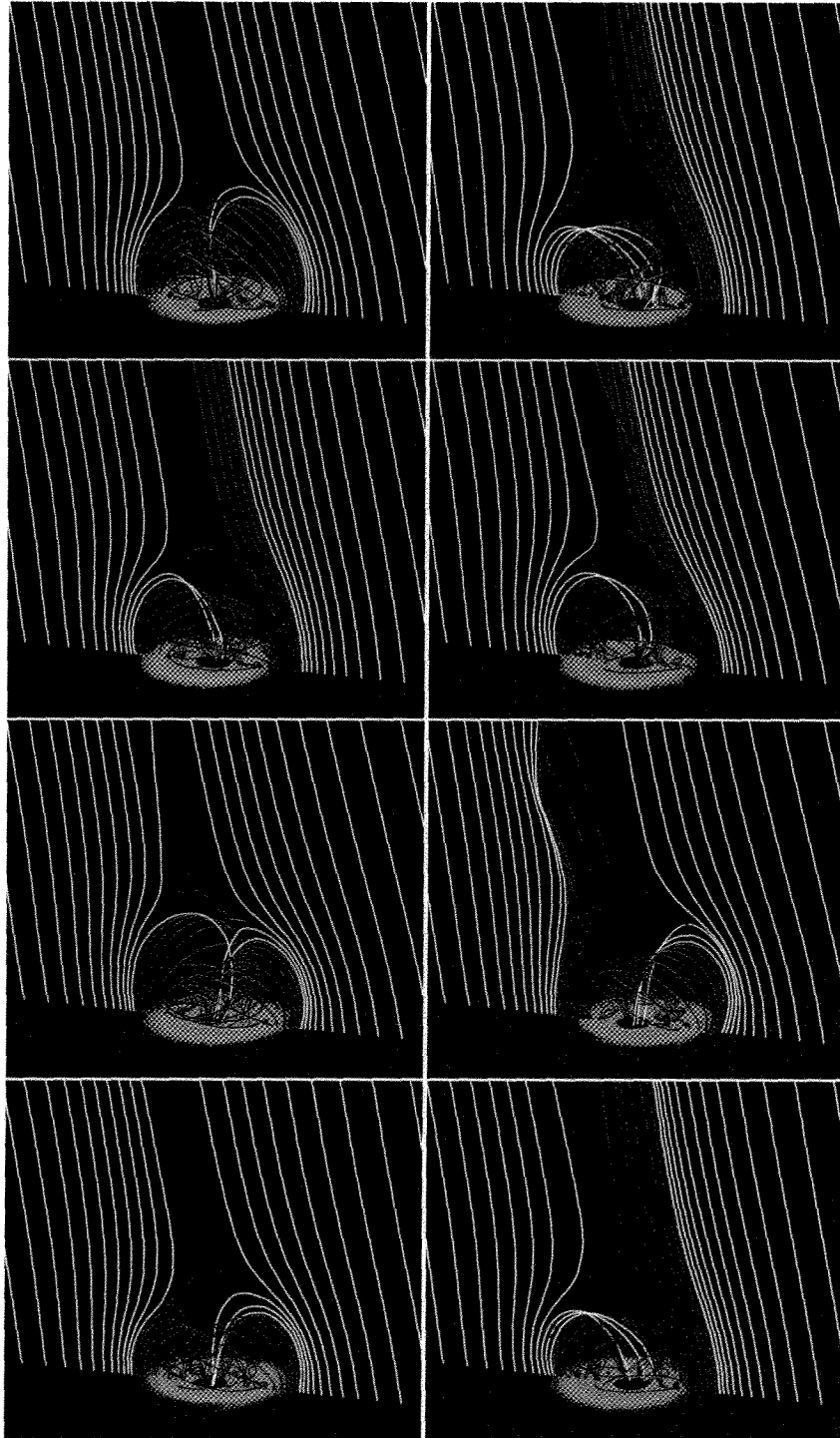
Fig. 5.— Evolution of the connectivity of the four jets (top to bottom) during the approach to (left column) and at the energy maximum $t_{\mathrm{Ef,max}}$ (right column) for each jet. In every panel, the 2D horizontal xy plane displays the distribution of $|\mathbf{B}|$ at the bottom boundary. Field lines are plotted from fixed positions along y at $z = 0$: red field lines belong initially to the closed domain, white field lines to the open domain. Black contour lines are isolevels of a 2D vertical cut at $x = 0$ of the electric current density.
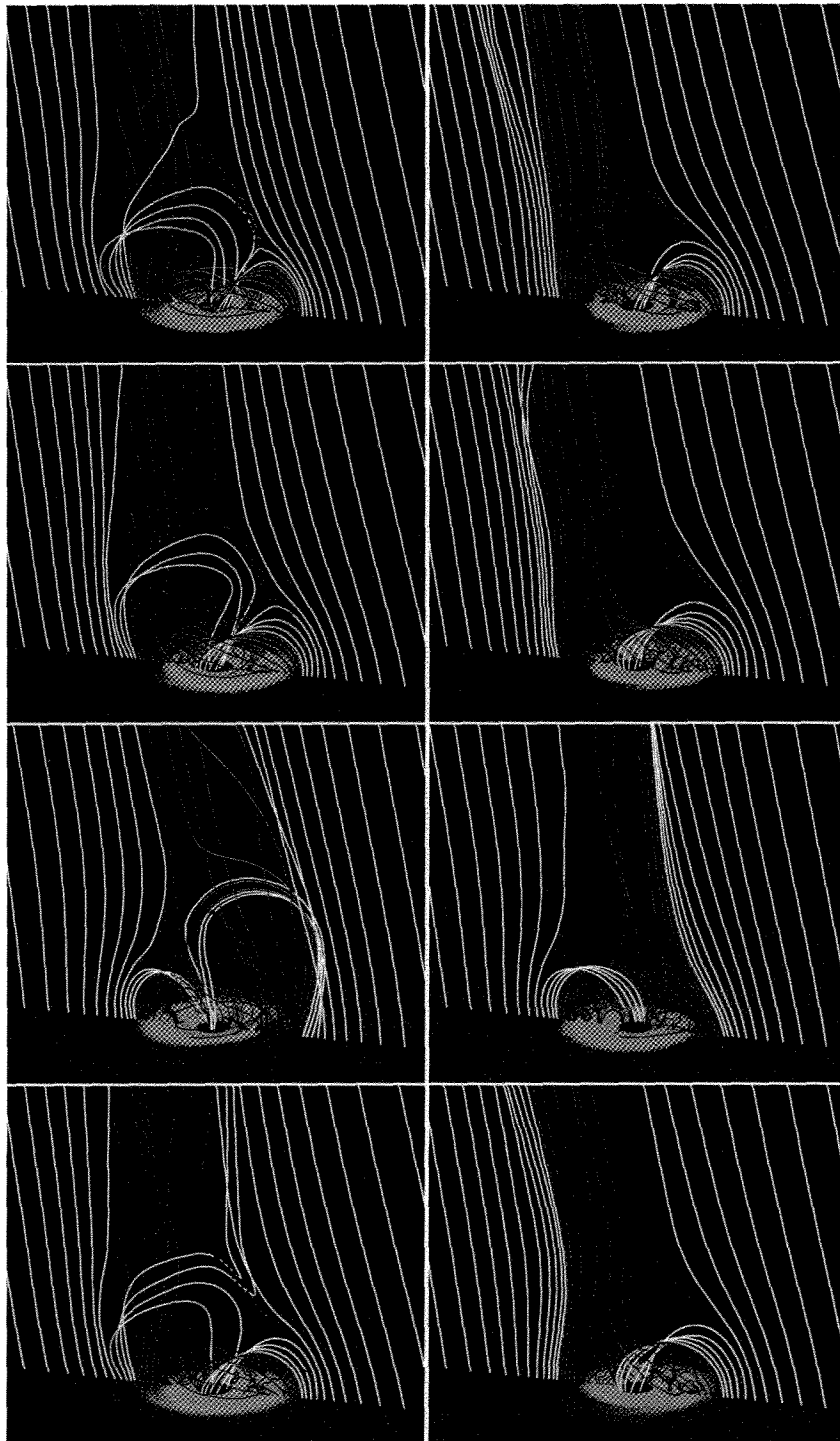
Fig. 6.— Evolution of the connectivity of the four jets (top to bottom) when the untwisting jet is triggered (left column) and after it is ejected (right column). See Figure 5 for a description of the items displayed in the panels.
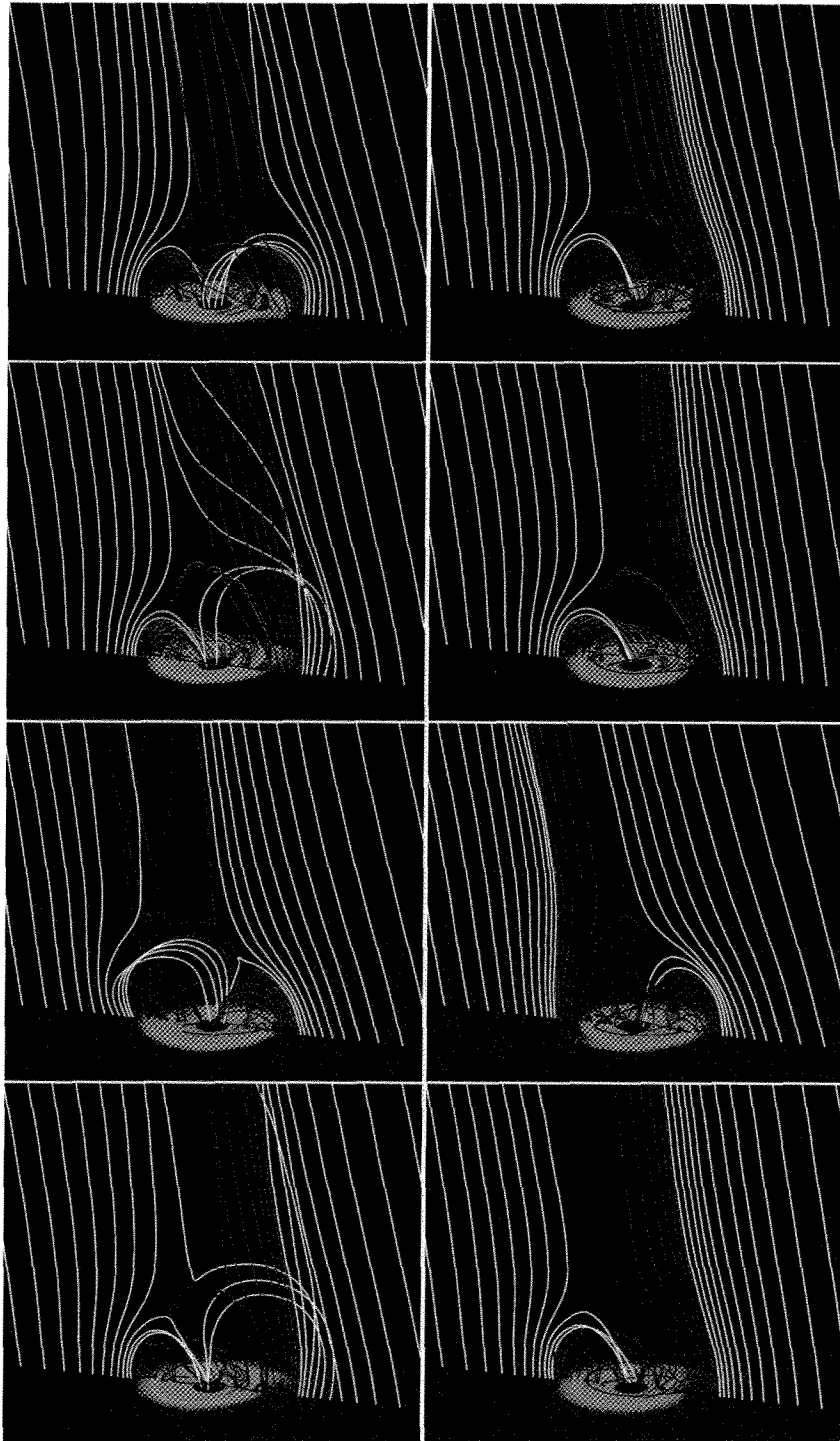
Fig. 7.— Evolution of the connectivity of the four jets (top to bottom) at the energy minimum $t_{\mathrm{Ef,min}}$ (left column) and later in the relaxed phase (right column). See Figure 5 for a description of the items displayed in the panels.
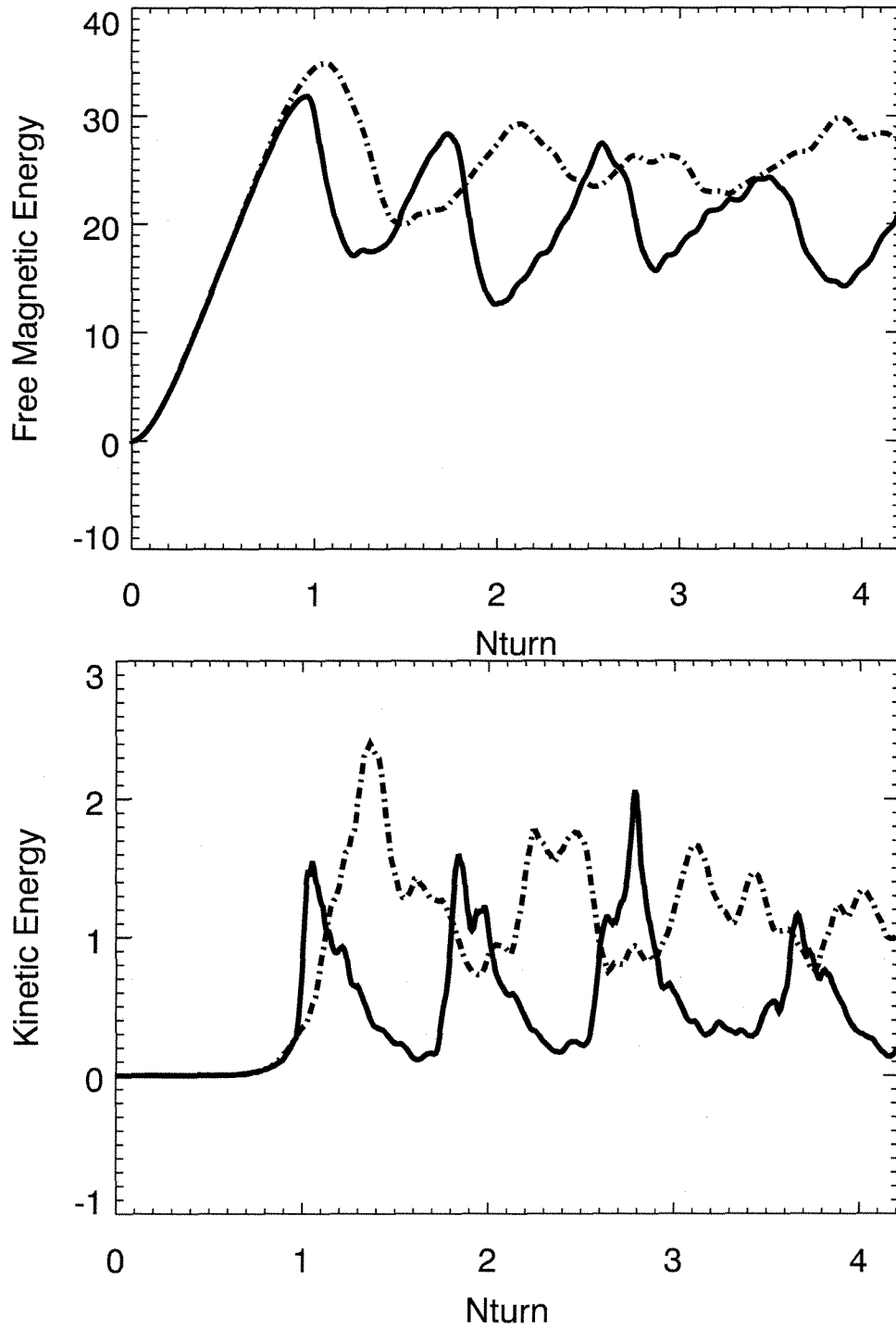
Fig. 8.— Evolution of the free magnetic (top panel) and kinetic (bottom panel) energies for the "slow" run 1 (*solid line*) and the "fast" run 2 (*dashed line*) versus the theoretical numbers of turns given to field lines anchored at radius $r = 1$.
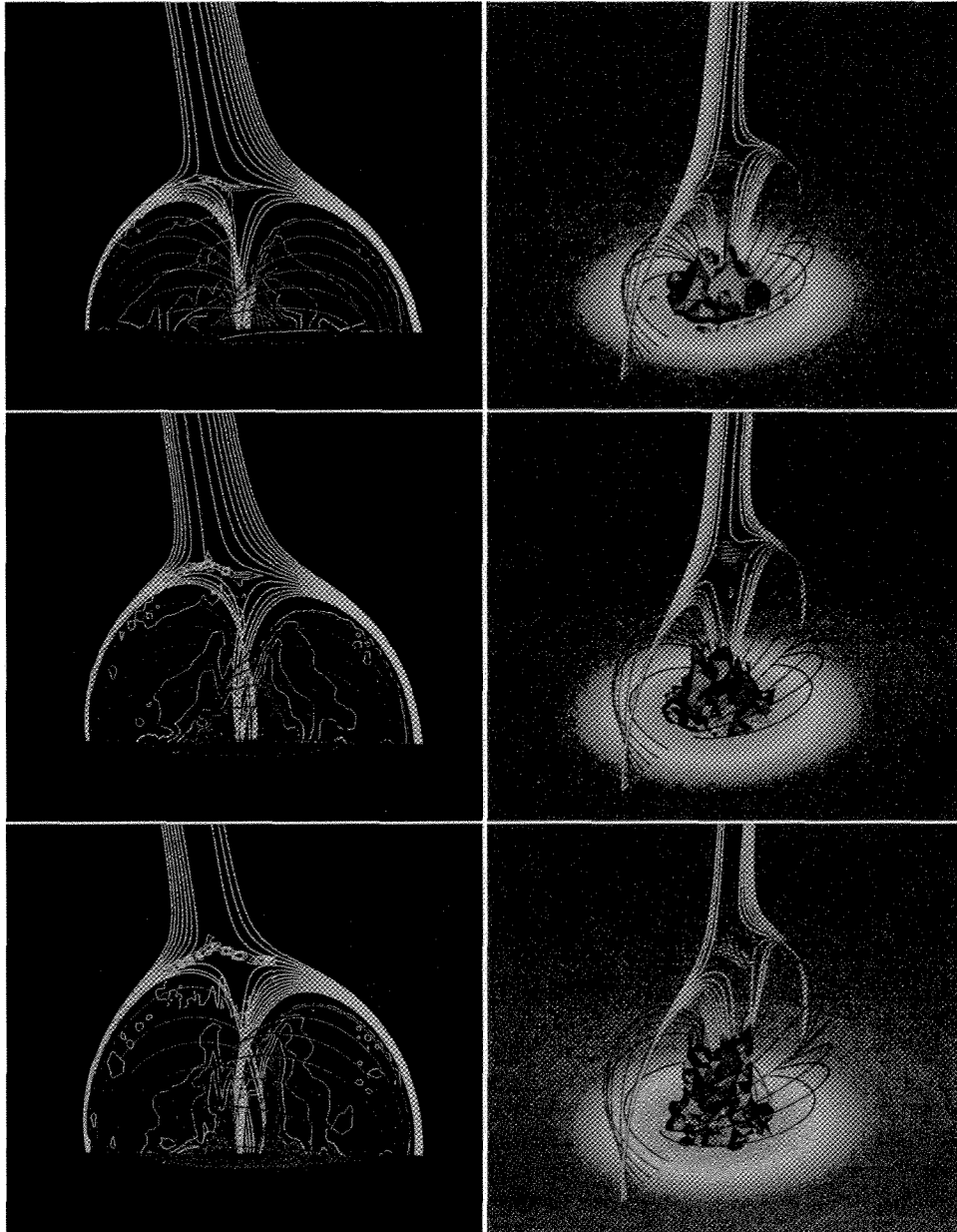
Fig. 9.— Side view (left column) and perspective view (right column) of the strengthening current sheet before onset of the first jet at times $t = 700$ (top panels), 850 (middle panels), 1000 (lower panels). The red field lines are those plotted in Figure 5; the pink field lines are plotted from fixed positions along two segments directed along $\pm y$ around the fan surface, mapping the evolution of the fan surface and fan separatrix. In the right column, the blue surface displays a 3D isolevel of the intense currents. In the left column, isocontours are drawn of the electric current density in the yz plane.
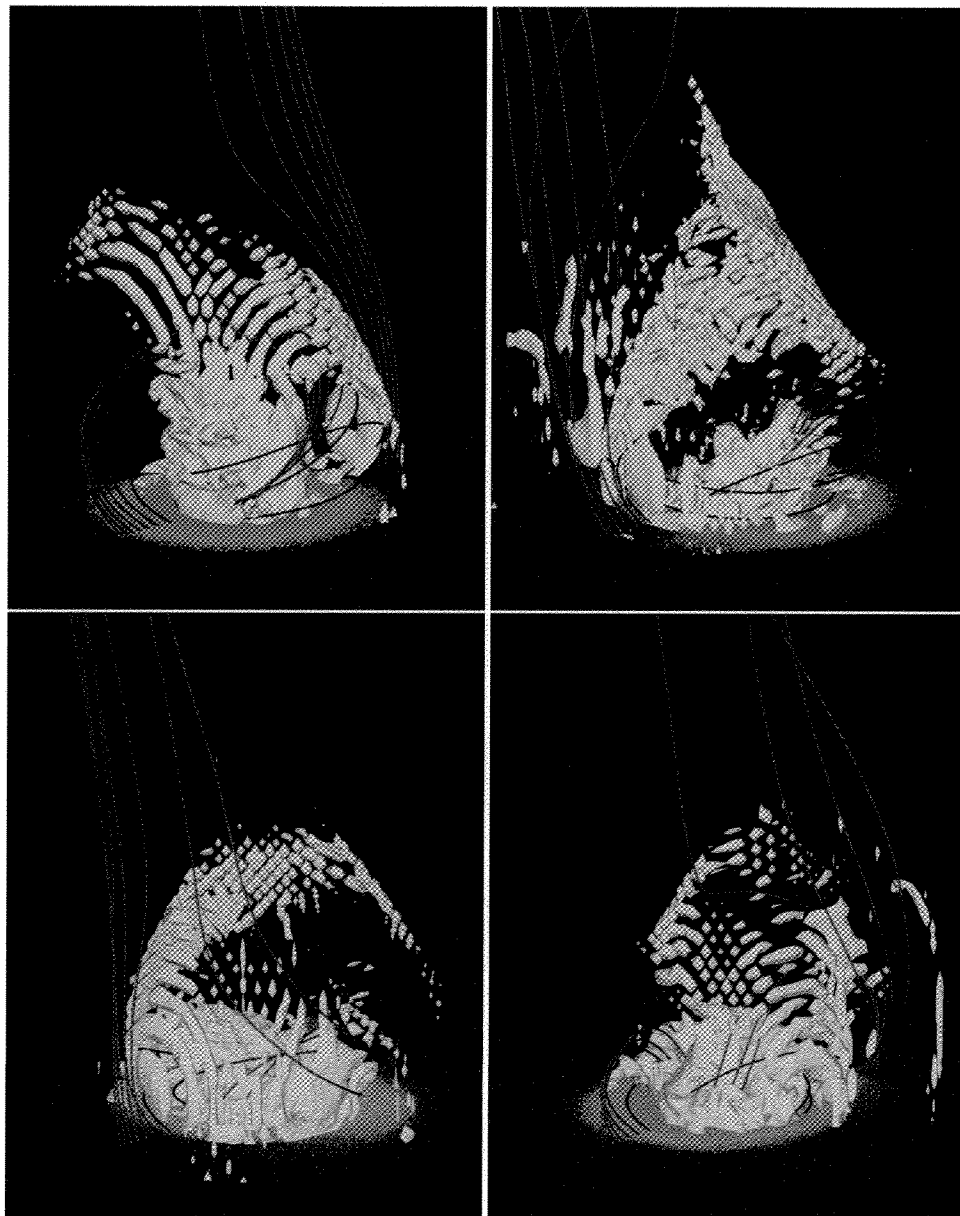
Fig. 10.— Evolution of the thin current sheet during the first jet at times $t = 1450$ (top left), 1550 (top right), 1650 (bottom left), and 1800 (bottom right). The red field lines are those plotted in Figure 5. The light blue surface displays a 3D isolevel of the intense currents.